Chapter 4

The Structural Performance of Stone-Masonry Bridges

George C. Manos, Nick Simos and
Evaggelos Kozikopoulos

Additional information is available at the end of the chapter

http://dx.doi.org/10.5772/64752

Abstract

The structural performance of old stone-masonry bridges is examined by studying such structures located at the North-West of Greece, declared cultural heritage structures. A discussion of their structural system is included, which is linked with specific construction details. The dynamic characteristics of four stone bridges, obtained by temporary *in situ* instrumentation, are presented together with the mechanical properties of their masonry constituents. The basic assumptions of relatively simple three-dimensional (3-D) numerical simulations of the dynamic response of such old stone bridges are discussed based on all selected information. The results of these numerical simulations are presented and compared with the measured response obtained from the *in situ* experimental campaigns. The seismic response of one such bridge is studied subsequently in some detail as predicted from the linear numerical simulations under combined dead load and seismic action. The performance of the same bridge is also examined applying 3-D non-linear numerical simulations with the results used to discuss the structural performance of stone-masonry bridges that either collapsed or may be vulnerable to future structural failure. Issues that influence the structural integrity of such bridges are discussed combined with the results of the numerical and *in situ* investigation. Finally, a brief discussion of maintenance issues is also presented.

Keywords: stone-masonry bridges, structural performance, *in situ* measurements, numerical simulations

1. Introduction

This chapter focuses on stone-masonry bridges that were built in Greece during the last 300 years and most of them survive today (**Figure 1a** and **b**).

Figure 1. (a) Konitsa Bridge, Ipiros, Greece and (b) Kokorou Bridge, Ipiros, Greece.

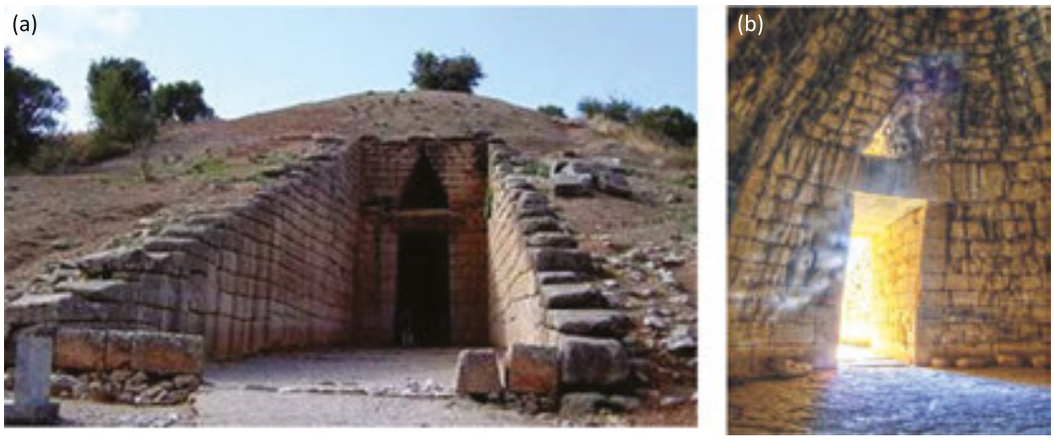

Figure 2. The royal tomb of Atreus at Mycenae in Peloponnese, Southern Greece.

The use of the stone-masonry arch that is utilized in forming stone-masonry bridges was extensively used in the times of the Roman Empire as part of the transportation system that was established and linked to various provinces of the Roman Empire. Evidence of stone-masonry arch bridges prior to Roman times is not known although stone-masonry structures in the East Mediterranean area for other uses date to prehistoric times. A well-known use of arch/vault stone-masonry structural form is the one that can be seen at the royal tombs, which have been excavated during the last 200 years in many places in Greece. In **Figure 2**, the royal tomb of Atreus at Mycenae, Greece, is depicted where stone masonry is employed to form an underground-vaulted structure with a diameter at its base of 14.60 m and a height of 13.30 m constructed with 33 subsequent series of stone masonry along the height.

The use of such vaulted stone-masonry structures demonstrates the efficient utilization of this structural form in order to bear efficiently the dead loads as well as the weight of the overlying soil volume in a state of stress dominated by compression (**Figures 2** and **3a**). On the contrary, the main gate of the royal palace walls at Mycenae in Peloponnese of Southern Greece (dated 1325 B.C. to 1200 B.C. and excavated 150 years ago), known as the gate of the lions (**Figure 3b**), uses the simple-supported beam-type structural system that characterizes most of the prehistoric and classical ancient Greek stone-masonry construction for above-the-ground

http://dx.doi.org/10.5772/64752

structures. The use of the stone-masonry arch/vault-type formation is also evident in the structural system of the royal tombs of the Macedonian kings at Vergina in Northern Greece, dated from 350 B.C. and excavated during the last 30 years (**Figure 3c** and **d**).

Figure 3. (a) Reconstruction of the royal tomb of Atreus, at Mycenae in Peloponnese, Southern Greece. (b) The gate of lions at Mycenae, Peloponnese, Southern Greece. (c) Reconstruction of the royal tomb of Philip, King of Macedonia at Vergina, Greece. (d) Interior of a Macedonian, royal tomb, Greece.

Figure 4. (a) Map of Macedonia with the location of the royal palaces at Vergina and Pella, Greece. (b) The remains of an ancient Roman bridge at a distance of 25 km from the Macedonian palaces of Vergina and Pella.

Despite the use of arch/vaulted stone-masonry structural formations for these underground Macedonian royal tombs at Vergina in Northern Greece, there is no evidence of such structural formations being used for bridges at that time. **Figure 4a** shows the location of the Macedonian royal palaces at Vergina and Pella in Northern Greece (red arrows).

In the same figure, the location of the remains of an ancient Roman bridge (blue arrow) is also indicated. These remains correspond today to only one main arch with a span of 15 m and a height of 7.5 m (**Figure 4b**). This surviving part of a Roman stone-masonry bridge is dated between 50 A.D. and 150 A.D. and, as can be seen in the map of **Figure 4a**, is located at a close distance (25 km) from the Macedonian palaces of Vergina and Pella as well as for the important cities of Thessaloniki and Dion (30–40 km). An inventory of Roman stone-masonry bridges is given by O'Connor [1]. These structures survive today, located in many European countries, having been in many cases preserved in good condition (**Figure 5a** and **b**) or partially collapsed in other cases (**Figure 5c** and **d**).

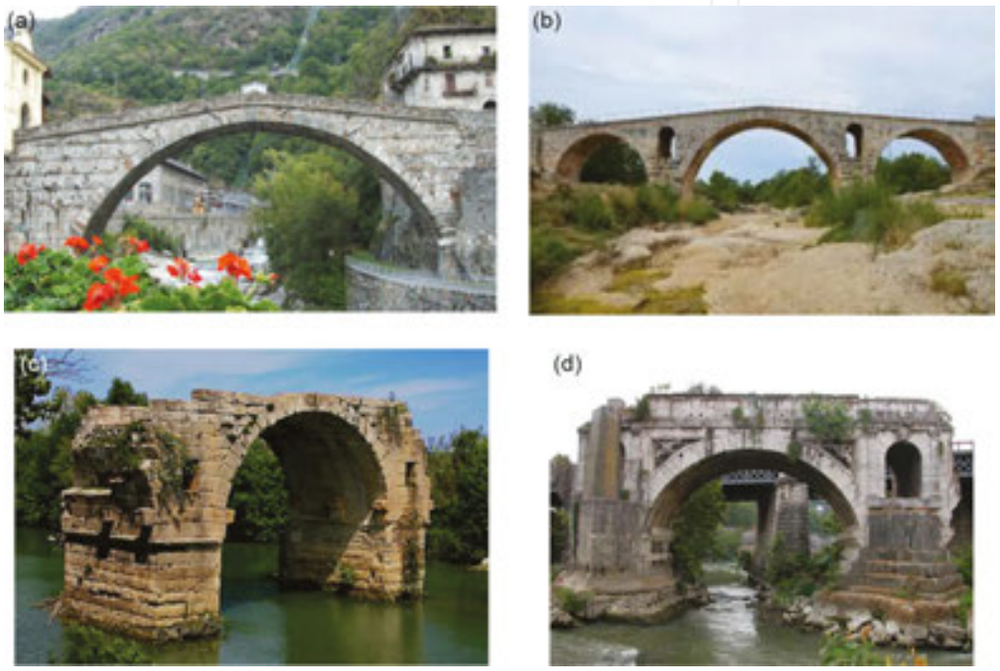

Figure 5. (a) Roman stone-masonry bridge Pont-Saint-Martin in Northern Italy. (b) The Pont Julien, a Roman stone arch bridge in the southeast of France, dating from 3 B.C. (c) The Pont Ambroix, first century B.C., Roman bridge in the south of France damaged by severe floods. (d) Ponte Rotto/Emilio, Rome (Broken/Emilio bridge). The remains of stone-masonry bridge damaged by flooding.

2. Geometric characteristics of the stone-masonry bridges located at North-West Greece

In what follows, a brief review is given of the basic geometric and construction characteristics of the stone-masonry bridges located at the far North-Western part of Greece called Ipiros. Bridges of similar geometric and construction characteristics are also located in other parts of Greece. The present study has selected the stone-masonry bridges that are located in Ipiros as they are numerous and are located in a relatively confined area that facilitates their temporary *in situ* instrumentation. The objective of this instrumentation, as explained in Section 4, is to measure their dynamic characteristics that represent a significant part of this study. All these

http://dx.doi.org/10.5772/64752

bridges, located in Ipiros as well as in other parts of Greece, have been documented, with relevant information included in [2]. Psimarni et al. [3] developed a geographic information system for the traditional bridges of Central Zagori, not yet accessible to the authors. Thus, all the geometric data utilized in this study were obtained through *in situ* measurements conducted by the authors.

Figure 6. (a) Kapetan Arkouda Bridge, Kipoi Village, East Zagori, Ipiros and (b) Agiou Mina Bridge, Kipoi Village, East Zagori, Ipiros.

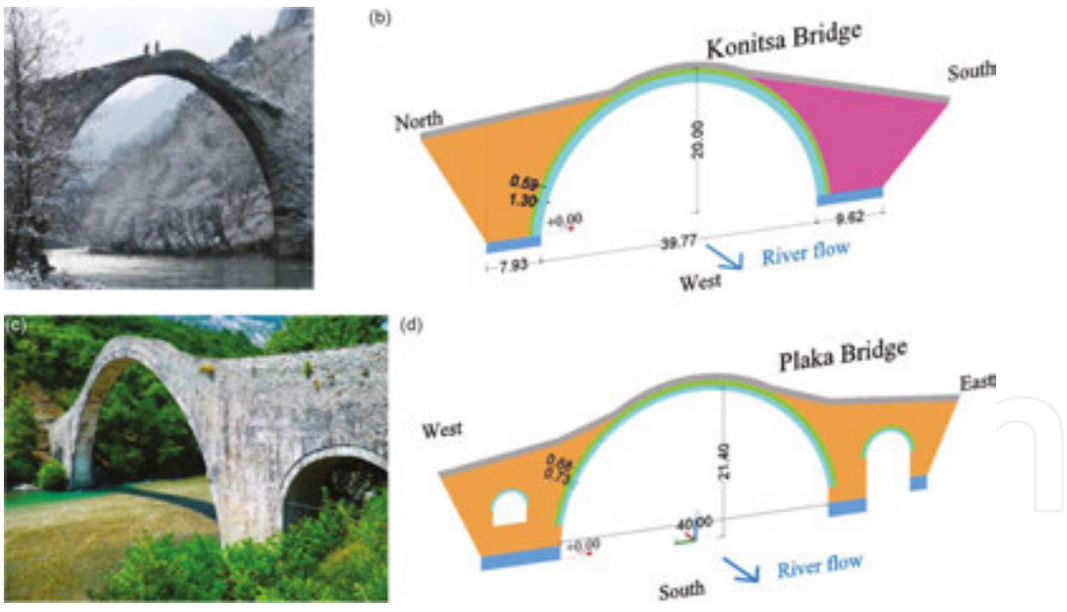

Figure 7. (a) and (b) Konitsa Bridge, Ipiros, Greece (width 2.85 m); (c) and (d) Plaka Bridge, Ipiros, Greece (width 3.10 m).

A considerable number of relatively small stone-masonry bridges can be found in this region with a span smaller than 10 m as the ones depicted in **Figure 6a** and **b**. However, stone-masonry bridges with a much larger total span have also been constructed. Relatively long-span stone bridges with a single central span are relatively few in number. The longest stone bridges with

one main central arch are the ones in Konitsa (**Figure 7a** and **b**) and the one in Plaka (**Figure 7c** and **d**). These stone-masonry bridges are very similar in the dimensions of the central arch, although the Arachthos river crossing by the Plaka Bridge is longer (75-m total span) due to adjacent additional arches at both ends (**Figure 7c**), whereas the main arch of the Konitsa Bridge is supported directly at the nearby slopes of the rocky Aoos river gorge. As will be presented briefly in Chapter 9 (see also figures 10g and 11 as well as section 7.3), the Plaka Bridge collapsed almost a year ago (31 January 2015). As can be seen in **Figure 7b** and **d**, the main central arch of both the Konitsa and the Plaka stone bridges has a clear span of nearly 40 m and a rise of 20 m.

Apart from the Plaka and Konitsa stone bridges, three more bridges will be examined in the present study. These stone bridges are depicted in **Figure 8a–f** and are namely the Kokorou Bridge, the Tsipianis Bridge and the Kontodimou Bridge. As can be seen in **Figure 8b** and **d**, the main central arch of the Kokorou Bridge has a clear span of 24.69 m and a rise of 12.71 m, whereas the Tsipianis Bridge has a clear span of 26.00 m and the rise 13.65 m. As can be seen, the central main arch of these two bridges has similar dimensions. Finally, the clear span of the Kontodimou Bridge is 14.50 m and the rise 7.40 m.

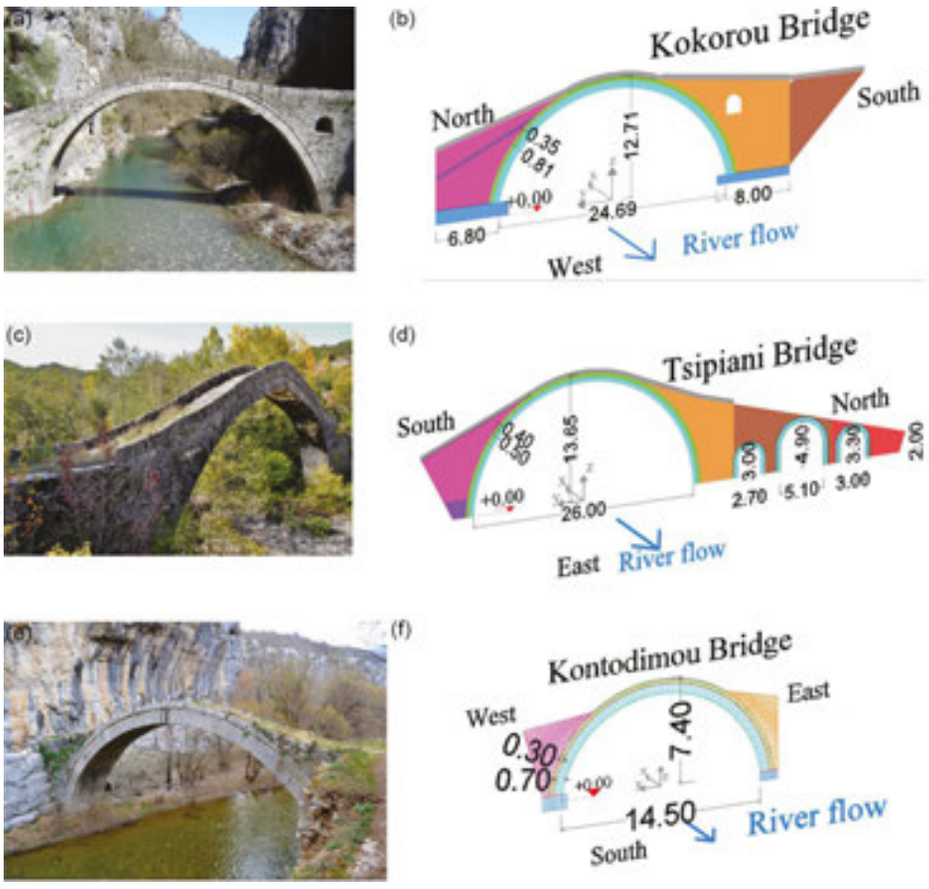

Figure 8. (a) and (b) Kokorou stone bridge, Kipoi Village, East Zagori, Ipiros (width 2.85 m); (c) and (d) Tsipianis stone bridge, Milotades Village, East Zagori, Ipiros (width 2.80 m); (e) and (f) Kontodimou stone bridge, Kipoi Village, East Zagori, Ipiros (width 2.77 m).

http://dx.doi.org/10.5772/64752

Thus, the present study covers stone bridges that are all dominated by a central main arch with a span/rise varying from 40.00/20.00 to 14.50/7.40 m. As can be seen in all cases, the clear span over rise ratio is close to 2.0 and the width is close to 3.0 m. In the cases of the longest span, the width of the structure increases as the arch approaches the foundation (Konitsa and Plaka Bridges). A distinct difference between the examined bridges is the fact that in the case of Konitsa, Kokorou and Kontodimou Bridges, the main arch is founded on abutments that are very close to the rocky slopes of the river gorge whereas for the Plaka and Tsipianis Bridges there is a mid-pier that is founded on the river bed together with adjacent smaller arches (**Figures 7d** and **8d**).

3. Construction characteristics

The construction characteristics of the various parts of these bridges are thought to bear some significance in the effort to understand the static, dynamic and earthquake behaviour of these structures. One can distinguish the following main structural components:

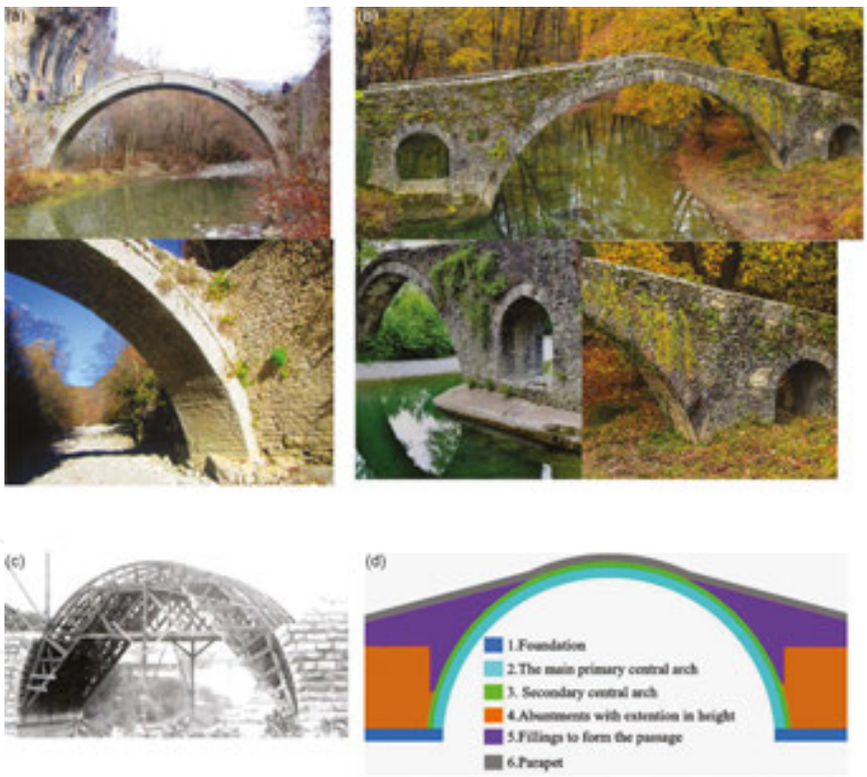

Figure 9. (a) Main central arch supported on the extension of the rocky part of the river bank at both ends; (b) main arch supported on right and left mid-piers which are also formed including adjacent arch; (c) wooden formwork for the support of the main central arch. Construction of the right and left abutments; and (d) construction of the main central arch preceded by the construction of the right and left abutments.

1. The main primary central arch is founded on abutments at either end of the bridge. These abutments are extensions of the rocky part of the river bank (**Figure 9a**). In the case of a

mid-pier, which was constructed on the dry part of the river bed, a separate foundation footing is constructed at a certain depth that is not easy to estimate. In case of relatively large river widths, the main arch was founded on right and left mid-piers that were also supporting adjacent arches as is seen in **Figure 9b**. A wooden formwork was employed to support the main arch during construction (**Figure 9c**).

2. The construction of the main central arch was preceded by the construction of its foundation at both ends together with the construction of the abutments that were raised up to a certain height in order to resist the thrust of the central arch.

3. The construction of the main central arch was followed in many cases with the construction of a secondary central arch on top of the main central arch (**Figures 9d** and **10a–f**).

4. Finally, the mandrel walls were constructed above the abutments in order to form together with the arches the main passage (deck) at the top of the bridge. In certain cases, this passage is protected at both sides at the deck level by an in-built continuous stone parapet that rises approximately 0.5 m above the deck level (**Figures 7a**, **c** and **8a**, **c**). In the case of the Kontodimou Bridge, this parapet is formed by individual stones in-built at intervals of approximately 1.6 m.

5. The thickness of the primary and secondary arches of the main span varies considerably. The primary arch for the Konitsa Bridge with a clear span of 40 m has a thickness of 1.30 m And The Secondary Arch A Thickness of 0.59 m (**Figures 7b** and **10a**). The primary arch of the Plaka Bridge again with a clear span of 40 m has a thickness of 0.73 m and the secondary arch a thickness of 0.68 m (**Figures 7d** and **10b**). The primary arch of the Kokorou Bridge with a clear span of 24.69 m has a thickness of 0.81 m and the secondary arch a thickness of 0.35 m (**Figures 8b**, **10c** and **d**). The primary arch of the Tsipiani Bridge with a clear span of 26 m has a thickness of 0.50 m and the secondary arch a thickness of 0.40 m (**Figure 8d**). Finally, the primary arch of the Kontodimou Bridge with a clear span of 14.5 m has a thickness of 0.70 m and the secondary arch a thickness of 0.30 m (**Figures 8f**, **10e** and **f**). These thickness values are approximate and correspond to the arch thickness at the maximum rise; in some cases, the primary and the secondary arch thicknesses vary having an increased thickness in the areas where these arches join the abutments.

6. The construction of both the primary and secondary main central arches as well as the rest of the arches was constructed with stones that were shaped in a very regular prismatic shape. In this way, the mortar joints of the masonry construction for these arches are relatively very small. The same holds for the foundation and the abutments up to a certain height. For these structural parts, according to oral tradition, special attention was paid for the quality of the stone and mortar to be employed.

7. On the contrary, neither the shape nor the quality of the stones or the mortar was of equal importance for the mandrel walls. As can be seen in **Figure 10g** that depicts the remaining part of the Plaka Bridge, these mandrel walls were internally constructed with some form of rubble. However, in order to protect these parts from the weather conditions, the mandrel walls were also encased within facades of good-quality stone masonry (**Figure 10g**).

http://dx.doi.org/10.5772/64752

8. Because the primary and secondary main arches were constructed at different construction stages, there is a continuous cylindrical joint that lies between them (see **Figure 10a–f**). As revealed by the remains of the collapsed Plaka Bridge, wooden beams with iron inserts were employed to connect the primary and secondary arches at certain intervals.

9. Iron ties were also used to connect the two opposite faces of the primary arch in many bridges. These iron ties are visible in the photos of the main central arch of the Plaka Bridge before its collapse and they are still in place at the parts of the arch that were salvaged after its collapse (**Figures 11** and **12**). The iron ties were also used to connect the opposite faces of the primary arch of the main span in Tsipianis Bridge (**Figure 13**) and in Voidomatis bridge at Klidonia (**Figure 14**).

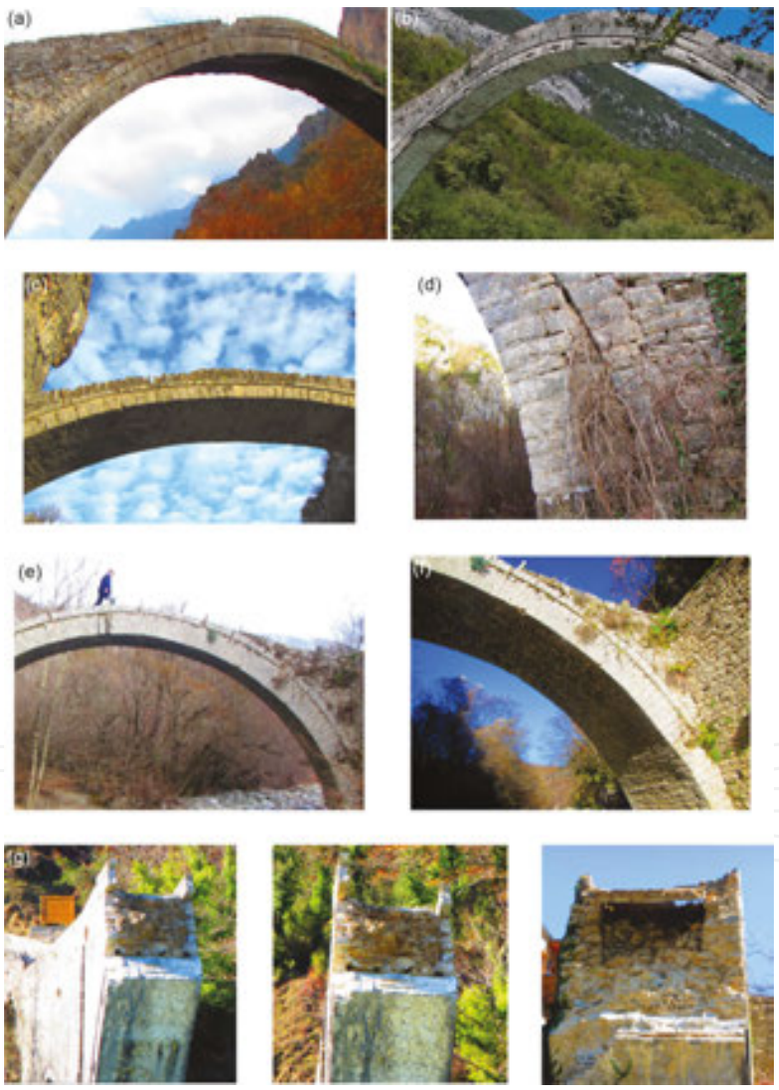

Figure 10. (a) Konitsa Bridge with the primary and secondary arches of the central span; (b) Plaka Bridge with the primary and secondary arches of the central span; (c) and (d) Kokorou Bridge with the primary and secondary arches of the central span; (e) and (f) Kontodimou Bridge with the primary and secondary arches of the central span; and (g) stone-masonry construction visible for the internal part of the mandrel walls of the remaining parts of Plaka Bridge.

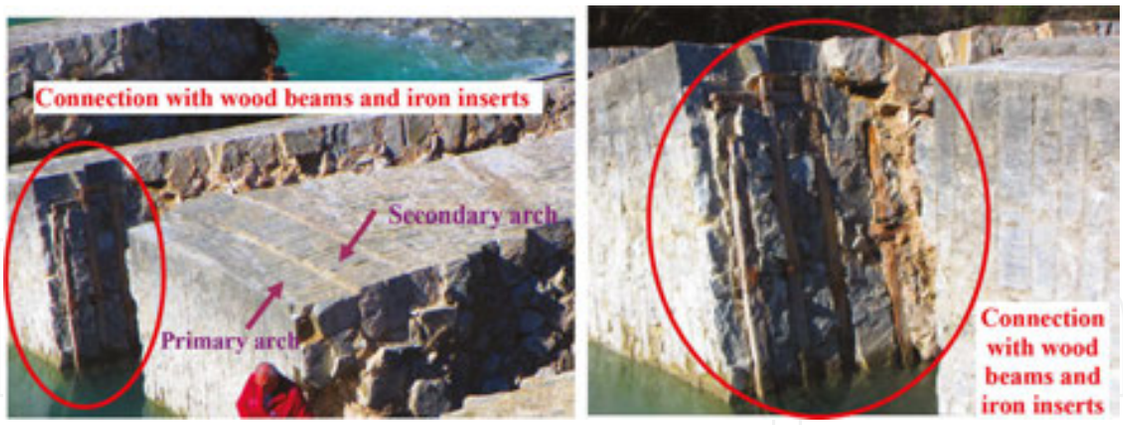

Figure 11. Connection with wooden beams and iron inserts between the primary and secondary arches of the Plaka Bridge.

Figure 12. Iron ties used to connect the two opposite faces of the primary arch in Plaka Bridge.

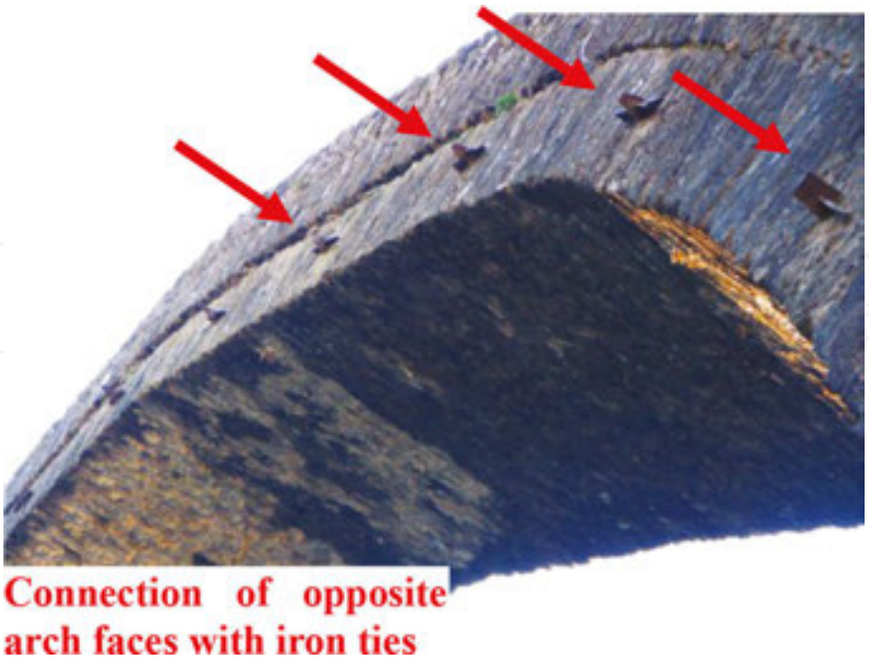

Figure 13. Iron ties used to connect the two opposite faces of the primary arch in Tsipianis Bridge.

http://dx.doi.org/10.5772/64752

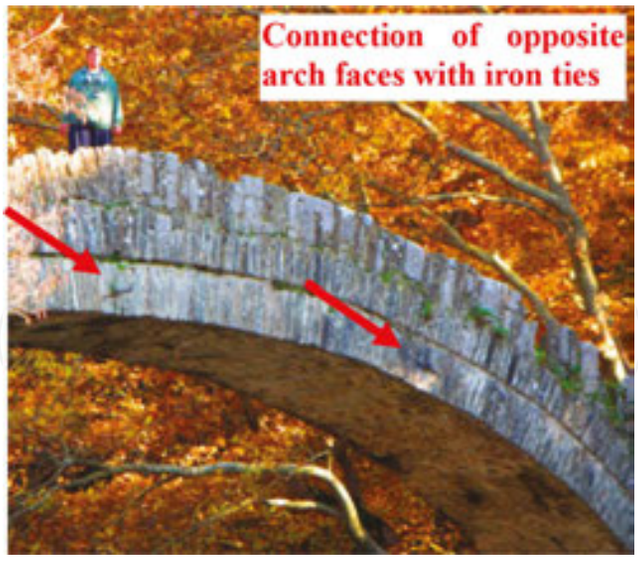

Figure 14. Iron ties used to connect the two opposite faces of the primary arch in Voidomatis Bridge.

4. *In situ* measurements of the dynamic characteristics of stone bridges

4.1. Four studied stone bridges

In measuring the dynamic response of four stone bridges, two types of excitation were mobilized. The first, namely ambient excitation, mobilized the wind, despite the variation of the wind velocity in amplitude and orientation during the various tests. Due to the topography of the areas where these stone bridges are located, usually a relatively narrow gorge, the orientation of the wind resulted in a considerable component perpendicular to the longitudinal bridge axis (**Figures 15a**, **17a**, **18a** and **19a**). This fact combined with the resistance offered to this wind component by the façade of each bridge produced sufficient excitation source resulting in small amplitude vibrations that could be recorded by the employed instrumentation. For this purpose, the employed SysCom triaxial velocity sensors had a sensitivity of 0.001 mm/s and a SysCom data acquisition system with a sampling frequency of 400 Hz. All the obtained data were subsequently studied in the frequency domain through available fast Fourier transform (FFT) software [4, 5]. This wind orientation relative to the geometry of each bridge structure coupled with the bridge stiffness properties could excite mainly the first symmetric out-of-plane eigen-mode, as can be seen in **Figure 16c** for the Konitsa Bridge. The variability of the wind orientation could also excite, although to a lesser extent, some of the other in-plane and out-of-plane eigen-modes (see **Figure 16c** for the Konitsa Bridge).

The second type of excitation that was employed, namely vertical in-plane excitation, was produced from a sudden drop of a weight on the deck of each stone-masonry bridge [6, 7]. This weight was of the order of approximately 2.0 kN that was dropped from a relatively small height of 100 mm, so as to avoid even the slightest damage to the stone surface of the deck of each bridge. Again, the level of this second type of excitation was capable of producing mainly

vertical vibrations and exciting the in-plane eigen-modes of each structure that could be captured by the employed SysCom triaxial velocity sensors with a sensitivity of 0.001 mm/s and a SysCom data acquisition system with a sampling frequency of 400 Hz. All the obtained data were subsequently studied in the frequency domain through available FFT software. In **Figure 15c**, the velocity measurements are depicted along the three axes (*x*-*x* horizontal out-of-plane, *y*-*y* horizontal in-plane and *z*-*z* vertical) as they were recorded during a typical sampling with the wind excitation. In **Figure 15d**, the velocity measurements are again depicted along the three axes (*x*-*x* horizontal out-of-plane, *y*-*y* horizontal in-plane and *z*-*z* vertical) as they were recorded during a typical sampling with the drop weight excitation. As can be seen, the drop weight excitation could produce at the dominant frequencies vibrations at least one order of magnitude larger than the wind excitation. From these measurements, an attempt was also made to obtain an estimate of the damping ratio for the dominant in-plane and out-of-plane frequencies. As is depicted in **Figure 16a** for the wind excitation, the main symmetric out-of-plane vibration that is excited by the wind has a dominant period of 2.539 Hz and a corresponding damping ratio approximately 1.7%. Similarly, as is depicted in **Figure**

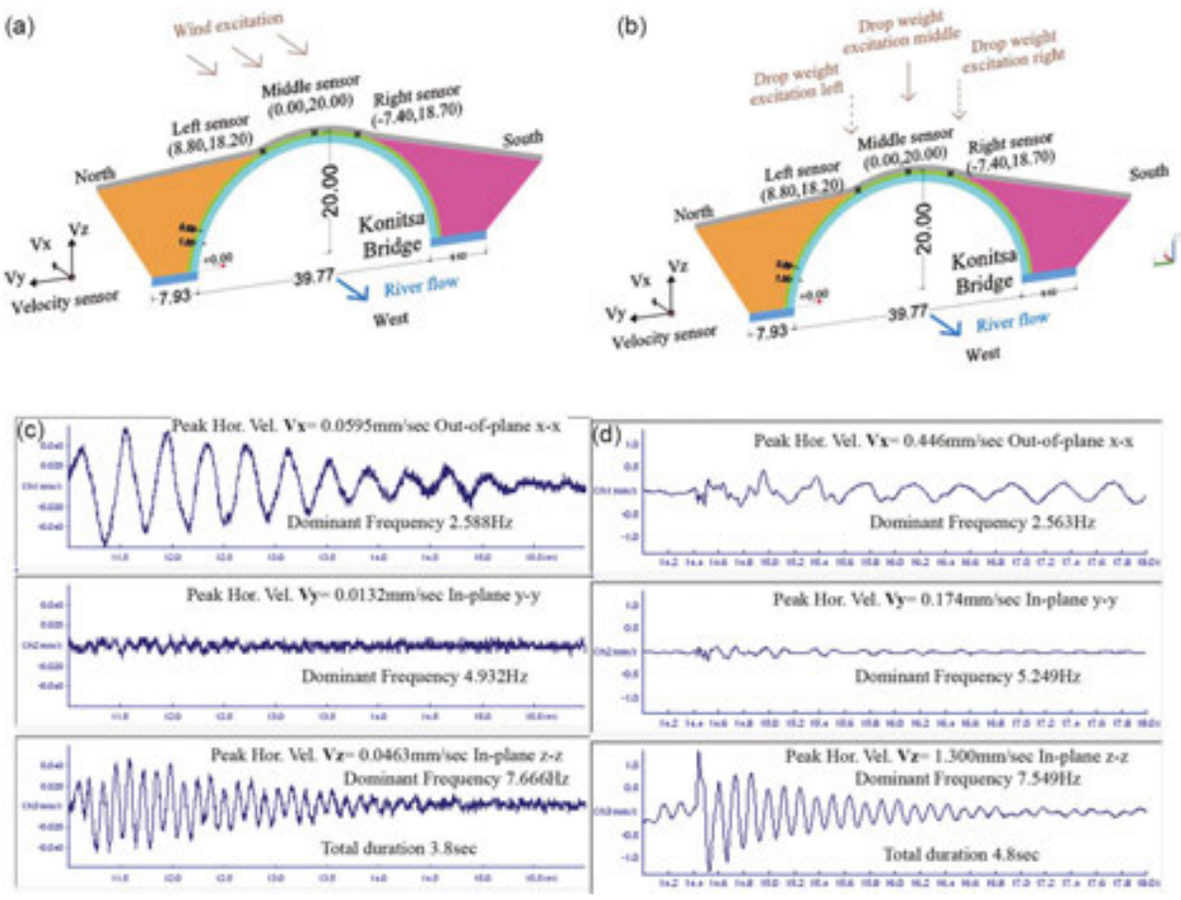

Figure 15. (a) Konitsa Bridge: wind excitation; (b) drop weight excitation; (c) vibration measurements from wind excitation recorded by the triaxial velocity sensor located at the crown of the Konitsa Bridge; and (d) vibration measurements from drop weight excitation at the crown of the bridge recorded by the triaxial velocity sensor located at the middle of the Konitsa Bridge.

http://dx.doi.org/10.5772/64752

16b for the drop weight excitation, the main symmetric in-plane vibration that is excited by the drop weight has a dominant period of 7.715 Hz and a corresponding damping ratio approximately 2.7%. This increase in the damping ratio value for this latter dominant frequency must be attributed to the relatively larger amplitudes of vibration that are produced from the drop weight excitation than from the wind excitation, as already underlined. All vibration measurements of the dynamic response of the Konitsa Bridge for either type of excitation were utilized to extract the eigen-frequencies depicted in **Figure 16c** together with the approximate shape of the corresponding eigen-modes.

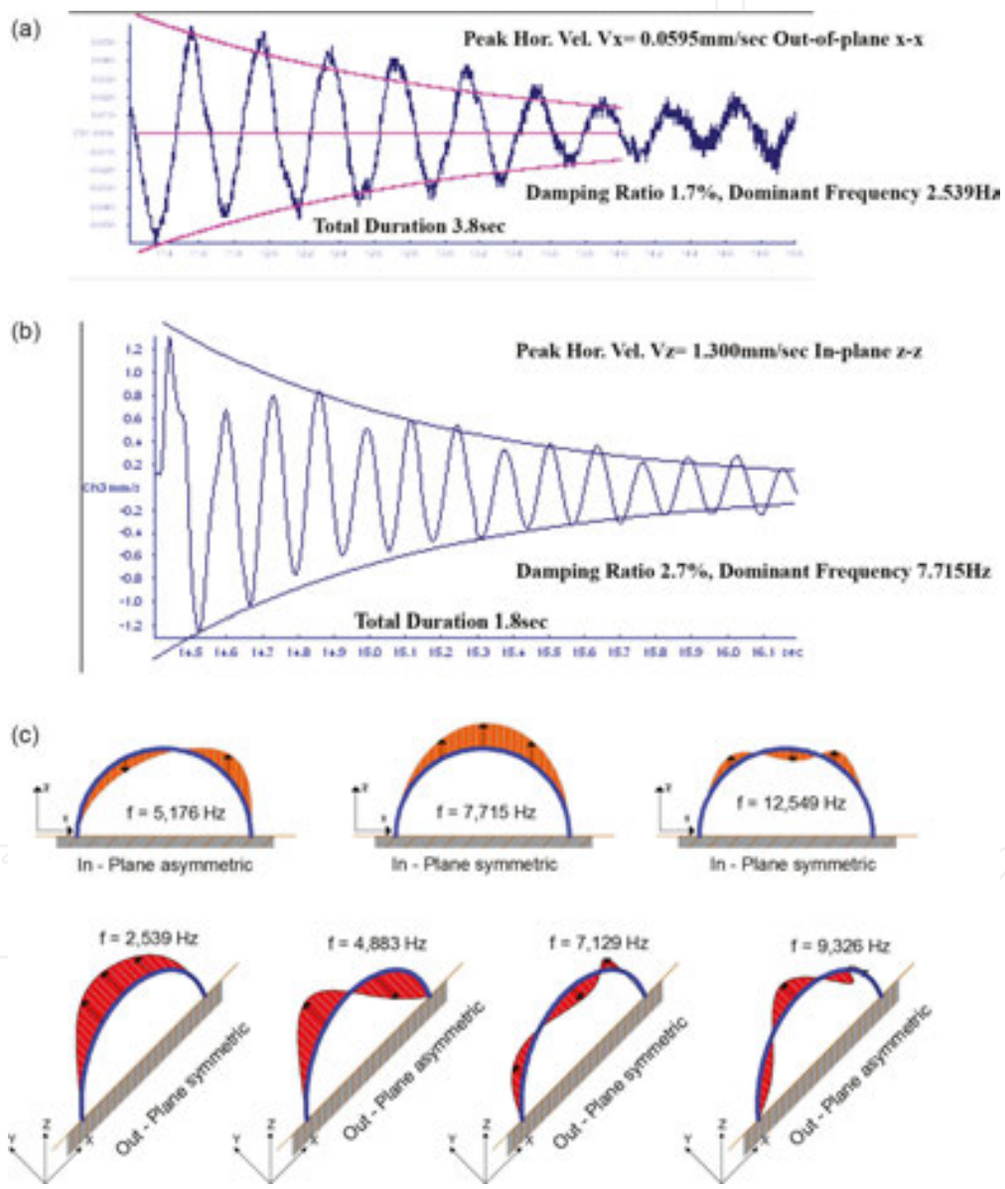

Figure 16. (a) Vibration measurements from wind excitation obtained from the triaxial velocity sensor located at the middle of the Konitsa Bridge; (b) vibration measurements from drop weight excitation at the middle of the bridge obtained from the triaxial velocity sensor also located at the middle of the Konitsa Bridge; and (c) measured eigen-frequencies and corresponding eigen-modes for the Konitsa Bridge.

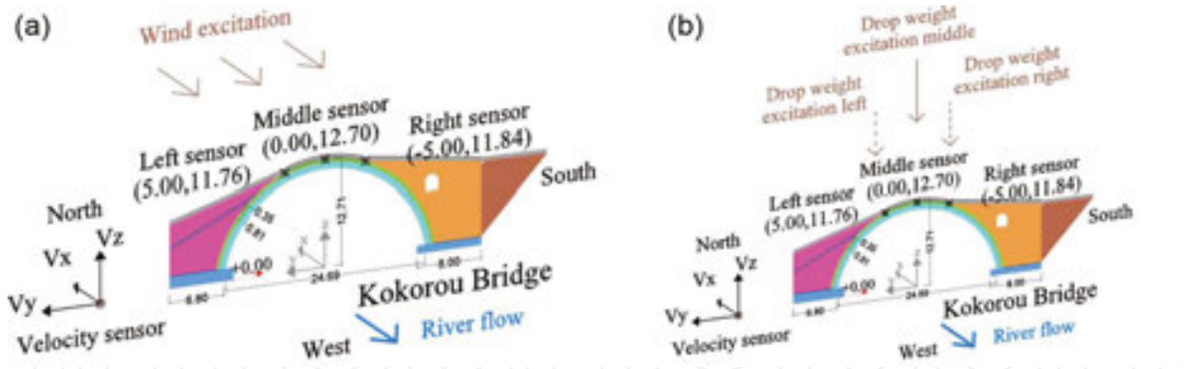

Figure 17. Kokorou Bridge: (a) wind excitation and (b) drop weight excitation.

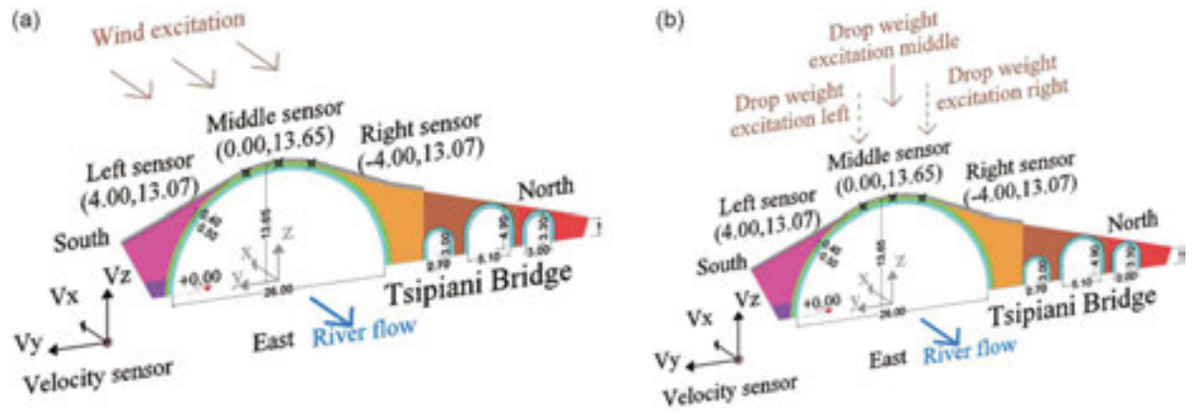

Figure 18. Tsipianis Bridge: (a) wind excitation and (b) drop weight excitation.

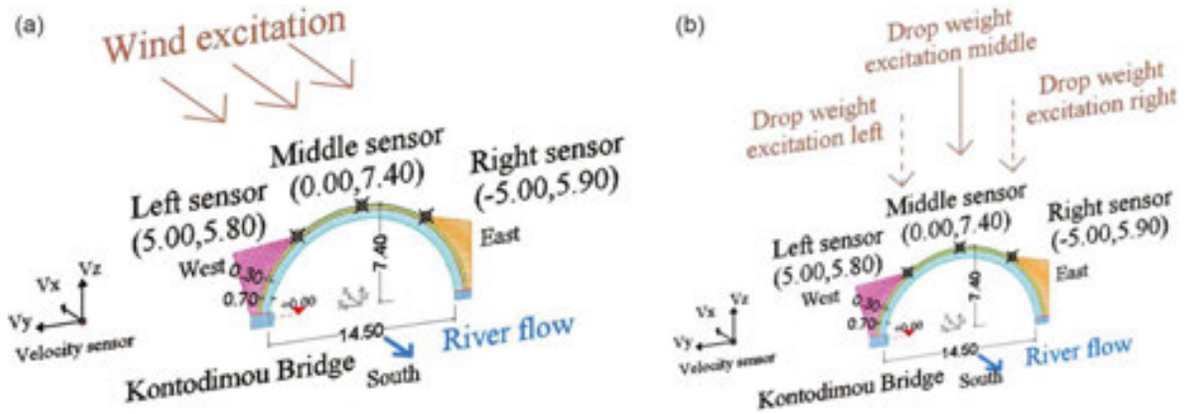

Figure 19. Kontodimou Bridge: (a) wind excitation and (b) drop weight excitation.

Measured eigen-frequencies (Hz) for the *Konitsa Bridge*			
In-plane	First asymmetric 5.176 Hz	Second symmetric 7.715 Hz	Third symmetric 12.549 Hz
Out-of plane	First symmetric 2.539 Hz	Second asymmetric 4.883 Hz	Third symmetric 7.129 Hz
Measured eigen-frequencies (Hz) for the *Kokorou Bridge*			
In-plane	First asymmetric 7.275 Hz	Second symmetric 10.059 Hz	Third symmetric 17.139 Hz
Out-of plane	First symmetric 4.541 Hz	Second asymmetric 7.471 Hz	Third symmetric 10.303 Hz
Measured eigen-frequencies (Hz) for the *Tsipiani Bridge*			
In-plane	First asymmetric 6.934 Hz	Second symmetric 8.549 Hz	Third symmetric 14.209 Hz
Out-of plane	First symmetric 3.320 Hz	Second asymmetric 6.348 Hz	Third symmetric 12.207 Hz
Measured eigen-frequencies (Hz) for the *Kontodimou Bridge*			
In-plane	First asymmetric 11.621 Hz	Second symmetric 16.934 Hz	Third symmetric 22.00 Hz
Out-of plane	First symmetric 7.860 Hz	Second asymmetric 16.846 Hz	Third symmetric 24.023 Hz

Table 1. Measured eigen-frequencies for four stone-masonry bridges.

The same process was followed for measuring the dynamic characteristics of another three stone-masonry bridges (Kokorou, Tsipianis and Kontodimou) using both the wind and the drop weight excitations, as shown in **Figures 17–19** where the position of the employed velocity sensors is indicated. Next, by utilizing all these vibration measurements of the dynamic response of each of these studied bridges for either type of excitation, it was possible to extract the relevant eigen-frequencies that are listed in **Table 1**. At least measurements of three repetitive sampling sequences for each type of excitation, either wind or drop weight, for each bridge (Konitsa, Kokorou, Tsipianis and Kontodimou) were measured. The eigen-frequency values listed in **Table 1** are values representing an average from corresponding values that were obtained by analysing the measured response from all tests.

4.2. Additional field measurements for the Konitsa Bridge

To gain more confidence in the *in situ* measurements presented in Section 4.1, the results of an independent *in situ* campaign are also presented here and briefly compared with the corresponding results presented in Section 4.1 for the same bridge. This additional *in situ* campaign was conducted during the end of October 2015 (**Figure 20**). This almost coincides with the *in situ* campaign described in Section 4.1, which was conducted during the period from mid-November 2015 till mid of December 2015 for all four bridges. Moreover, for the Konitsa Bridge the measurements presented in Section 4.1 were obtained on the dates of 8, 16 and 20 November. Based on this timing and the constant weather conditions prevailing during this period, no influence is expected to arise from environmental conditions to all these measurements. The objective of this independent field experiment was the same, that is, to assess the dynamic characteristics of the Konitsa stone arch bridge [8] using a set of Wilcoxon high-sensitivity accelerometers (1000 V/g) integrated with a data-recording/FFT analyzer RION-S78 system depicted in **Figure 20**. Further data post-processing was performed using a set of additional FFT processing software.

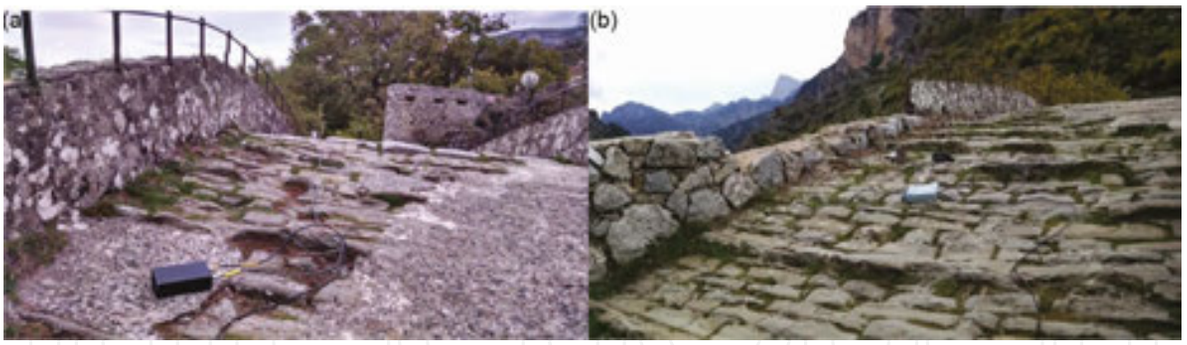

Figure 20. RION system and accelerometer system used in Konitsa Bridge field study. (a) Location of sensor at the South part of Konitsa Bridge and (b) location of the sensor at the North part of Konitsa Bridge.

Shown in **Figure 21** are the post-wind gust bridge response (vertical acceleration) and the corresponding power spectrum associated with the trace segment between 12 and 16 s of the record [4]. The power spectrum associated with the decay segment clearly delineates (a) the symmetric vertical mode (7.75 Hz).

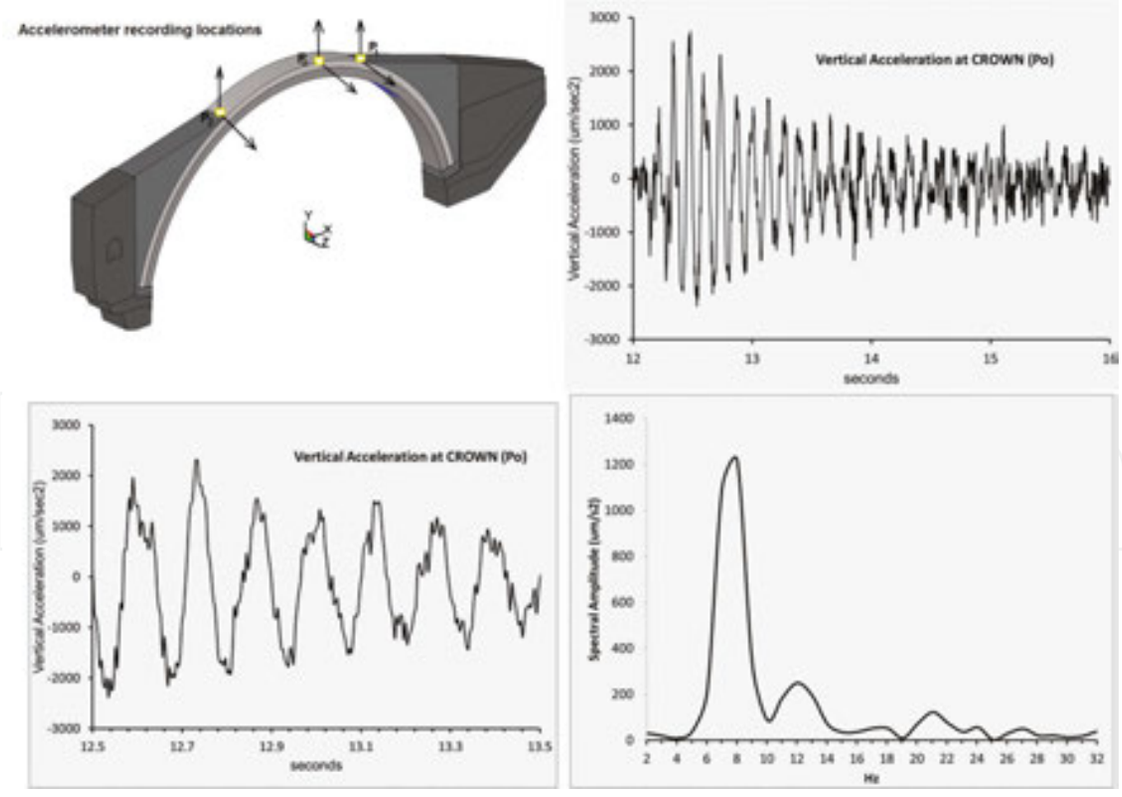

Figure 21. Decay segment of acceleration trace (vertical) and the corresponding power spectrum (7.75 Hz, damping ratio estimate of 1.6%).

http://dx.doi.org/10.5772/64752

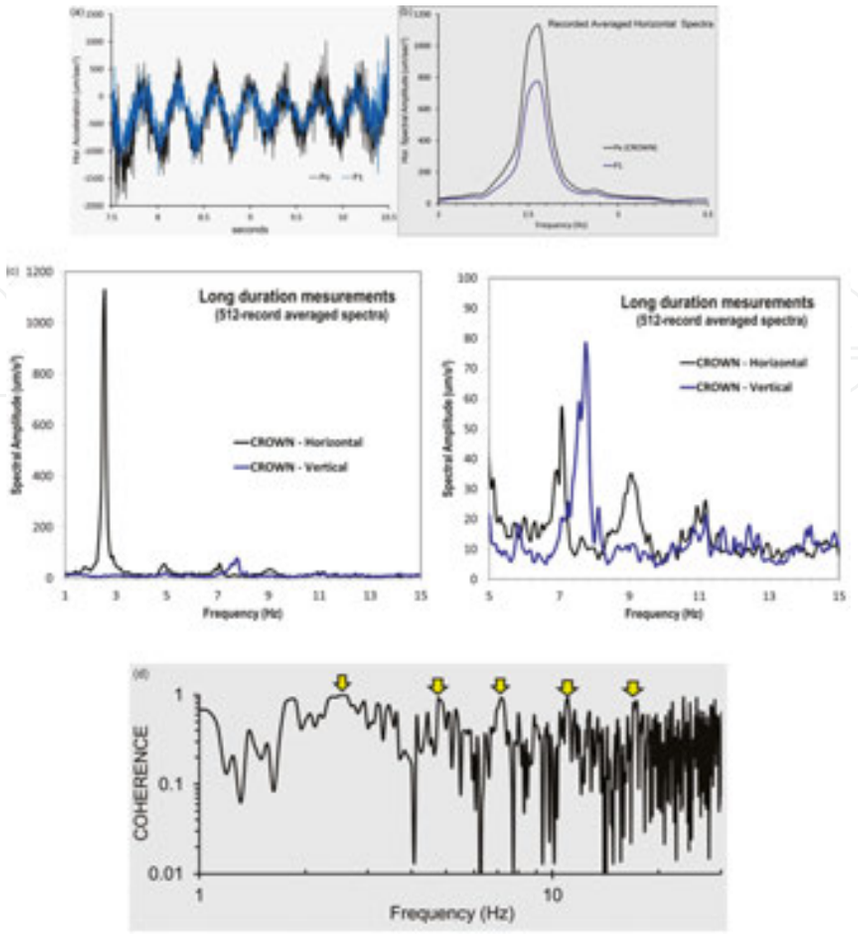

Figure 22. Horizontal (out-of-plane) acceleration time histories recorded simultaneously at two locations on the Konitsa Bridge deck. (a) Entire trace including high wind effects; (b) post-wind free vibration. Dominant frequency of 2.56 Hz; (c) recorded vertical and horizontal spectra at crown averaged over 512 records; (d) coherence measurements between P_o and P_1 locations aiding mode identification (arrows indicate 100% coherence characteristic of the structure modes).

Figure 22 depicts the horizontal (out-of-plane) acceleration time histories recorded simultaneously at two locations on the Konitsa Bridge deck and their corresponding power spectrum with dominant frequency of 2.56 Hz (first out-out-of plane eigen-mode). Comparing the eigen-frequency values obtained for the *in situ* experiments, reported in Section 4.1 (depicted in **Figures 15** and **16**), with the corresponding values obtained from this independent *in situ* experiments (depicted in **Figures 21** and **22**), very good consistency can be observed. **Figure 22c** and **b** depict the FFT-averaged Fourier spectral curves that formed the base together with the coherence plot of **Figure 22d** to identify with confidence the eigen-frequency values [9].

5. Laboratory tests for the stone masonry

A laboratory testing sequence was performed having as an objective to study in a preliminary way the mechanical characteristics of the basic materials representative of the materials

employed to build the studied stone-masonry bridges [4]. For this purpose, stone samples were selected from the neighbourhood of the collapsed Plaka Bridge as well as from a quarry near the Kontodimou and Kokorou Bridges. Moreover, stone samples were also taken from the river bed of the Kontodimou Bridge. Furthermore, it was possible to take a mortar sample from the collapsed Plaka Bridge. From both the stone and mortar samples collected *in situ*, it was possible to form specimens of regular prismatic geometry. These specimens were subjected to either axial compression or four-point bending tests. For the compression tests, the loaded surfaces of the prisms were properly cupped. **Figure 23a** and **c** depict typical loading arrangements employed for the compression (stone and mortar specimens) tests, whereas **Figure 23b** depicts the loading arrangement employed for the four-point bending tests. The applied load was measured through a load cell and the deformation of the tested specimens was measured employing a combination of displacement sensors as well as a number of strain gauges. These measurements were continuously recorded with a sampling frequency of 10 Hz. Through these measurements, the mechanical characteristics of the tested specimens were obtained in terms of compressive strength, flexural tensile strength, Young's modulus of elasticity and Poisson's ratio. The obtained values of these mechanical parameters are listed in **Tables 2–6**.

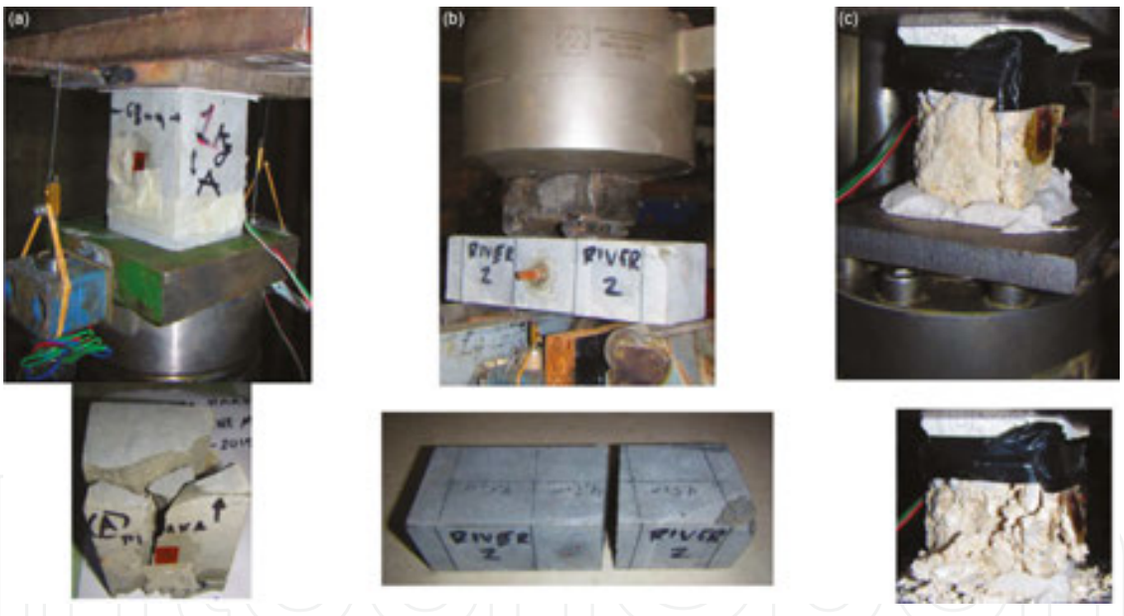

Figure 23. (a) Testing in compression stone samples taken from Plaka Bridge; (b) testing in four-point flexure stone sample taken from the river bed of Kontodimou Bridge; and (c) testing in compression mortar samples taken from Plaka Bridge.

Code name of sample	Cross section (mm^2)	Height (mm)	Maximum load (KN)	Compressive strength (MPa)	Slenderness ratio*/correction coefficient	Compressive strength (MPa) with correction due to slenderness*
River 1a	58.5 × 48.5	74.0	310.2	124.0	1.383/0.82	101.7
River1b	61.5 × 48.3	61.0	230.5	77.6	1.111/0.70	54.3

http://dx.doi.org/10.5772/64752

Code name of sample	Cross section (mm^2)	Height (mm)	Maximum load (KN)	Compressive strength (MPa)	Slenderness ratio*/correction coefficient	Compressive strength (MPa) with correction due to slenderness*
River 2a	56.3 × 45.0	59.5	225.6	89.0	1.175/0.73	65.0
River 2b	59.0 × 45.0	65.5	363.0	136.0	1.260/0.77	104.7
River 2c	33.0 × 65.0	59.0	220.7	102.9	1.205/0.75	77.2
Kontodimou Bridge River stone			**Average compressive strength** ** **= 80.6 MPa,** E_1 **= 55,560 MPa,** ν **= 0.259**			
Quarry 1a	55.0 × 45.5	70.0	416.9	166.6	1.394/0.82	136.6
Quarry 1b	52.0 × 46.0	73.5	230.5	96.4	1.500/0.90	88.8
Quarry 2a	44.8 × 44.8	84.5	193.3	96.3	1.886/0.95	91.5
Quarry 2b	47.0 × 44.8	43.5	313.9	149.0	0.948/0.65	96.9
Kontodimou Bridge Quarry stone			**Average compressive strength** ** **= 103.5 MPa,** E_1 **= 85,000 MPa,** ν **= 0.3**			

*Reference slenderness ratio = 2.0.
**The average compressive strength refers to a prism with a slenderness ratio = 2.

Table 2. Compression tests (22 January 2016) with stone samples taken near Kontodimou Bridge.

Code name of sample	Width (mm)	Height (mm)	Span (mm)	Maximum vertical load (kN)	Tensile strength (MPa)	Young's Modulus from flexure (MPa) (DCDT)
River 1	60.0	46.5	135.0	24.98	23.41	2875
River 2	60.0	45.0	135.0	22.66	25.18	1545
Kontodimou Bridge River stone			**Average tensile flex. strength = 24.30 MPa,** E_2 **= 2210 MPa**			
Quarry 1	54.0	46.5	135.0	12.875	14.89	11,205
Quarry 2	45.0	44.5	135.0	13.647	20.67	15,345
Kontodimou Bridge Quarry stone			**Average tensile flex. strength = 17.78 MPa,** E_2 **= 13,275 MPa**			

Table 3. Flexure tests (15 January 2016) with stone samples taken near Kontodimou Bridge.

Code name of sample	Cross section (mm^2)	Height (mm)	Maximum load (kN)	Compressive strength (MPa)	Slenderness ratio*/ correction coefficient	Compressive strength (MPa) with correction due to slenderness*
Specimen A	61.0 × 68.0	93.0	264.9	63.9	1.442/0.87	55.6
Specimen B	67.5 × 62.0	89.0	443.4	106.0	1.375/0.82	86.9
Plaka Bridge stone Specimens			**Average compressive strength** ** **= 71.3 MPa,** E_1 **= 40,000 MPa,** ν **= 0.142**			

*Reference slenderness ratio = 2.0.
**The average compressive strength refers to a prism with a slenderness ratio = 2.

Table 4. Compression tests (18 December 2015) with stone samples taken at Plaka Bridge.

Code name of sample	Width (mm)	Height (mm)	Span (mm)	Maximum vertical load (kN)	Tensile strength (MPa)	Young's Modulus from flexure (MPa) (S.G.)
Specimen A	52.0	52.0	180.0	14.75	18.88	33,330
Specimen B	52.0	52.0	180.0	12.13	15.52	36,360
Plaka Bridge stone specimens			**Average tensile flex. strength = 17.20 MPa, E_2 = 34,845 MPa**			

Table 5. Flexure tests (18 December 2015) with stone samples taken at Plaka Bridge.

Code name of sample	Cross section (mm^2)	Height (mm)	Maximum load (kN)	Compressive strength (MPa)	Slenderness ratio*/ correction coefficient	Compressive strength (MPa) with correction due to slenderness*
Specimen 1	27.5 × 57.0	66.0	3.228	2.06	1.562/0.91	1.875
Plaka Bridge stone specimens			**Compressive strength = 1.875 MPa, E_1 = 2500 MPa, ν = 0.35**			

Table 6. Compression tests (28 January 2016) with mortar samples taken at Plaka Bridge.

6. Numerical simulation of dynamic characteristics

In this section, the dynamic characteristics of the four studied stone-masonry bridges will be predicted through a numerical simulation process. Initially, this numerical simulation will be based on elastic behaviour, assuming the stone masonry as an orthotropic continuous medium and limiting these numerical models at approximately the interface between the end abutments and the rocky river banks, thus introducing boundaries at these locations [10]. For simplicity purposes, the bulk of these numerical simulations are made in the 3-D domain representing these bridge structures with their mid-surface employing thick-shell finite elements [11]. The various main parts of these stone-masonry bridges, that is, the primary and the secondary arches, the abutments, the deck, the mandrel walls and the parapets, were simulated in such a way that narrow contact surfaces could be introduced between them, representing in this way a different 'softer' medium. All available information, measured during the *in situ* campaign, on the geometry of each one of these parts for every bridge was used in building up these numerical simulations. The mechanical property values obtained from the stone and mortar sample tests, which were presented in Section 5, indicate the following main points. Young's modulus of the stone samples in axial compression has a value exceeding 40 GPa, whereas they yield a much less stiff behaviour in flexure. It is well known that the complex triaxial behaviour of masonry cannot be easily approximated from the mechanical behaviour of its constituents. For the studied stone-masonry bridges, this becomes even more difficult considering the various construction stages that were discussed in Section 3, the variability of the materials employed to form the distinct parts during these construction stages and the interconnection and contact conditions between the various parts formed during

http://dx.doi.org/10.5772/64752

these construction stages (abutments, primary and secondary arches, deck, parapets, mandrel walls). Moreover, there is important information that is needed in order to form with some realism the boundary conditions at the river bed and banks [11]. The lack of specific studies towards clarifying in a systematic way all these uncertainties represents a serious limitation in the numerical simulation process.

Measured/predicted eigen-frequencies (Hz) for the ***Konitsa Bridge***			
In-plane	First asymmetric 5.176/6.724	Second symmetric 7.715/7.076	Third symmetric 12.549/10.065
Out-of plane	First symmetric 2.539/2.432	Second asymmetric 4.883/4.478	Third symmetric 7.129/7.275
Measured eigen-frequencies (Hz) for the ***Kokorou Bridge***			
In-plane	First asymmetric 7.275/10.212	Second symmetric 10.059/11.134	Third symmetric 17.139/15.125
Out-of plane	First symmetric 4.541/4.035	Second asymmetric 7.471/7.065	Third symmetric 10.303/11.545
Measured eigen-frequencies (Hz) for the ***Tsipiani Bridge***			
In-plane	First asymmetric 6.934/7.106	Second symmetric 8.549/10.029	Third symmetric 14.209/12.742
Out-of plane	First symmetric 3.320/3.090	Second asymmetric 6.348/5.734	Third symmetric 12.207/9.248
Measured eigen-frequencies (Hz) for the ***Kontodimou Bridge***			
In-plane	First asymmetric 11.621/11.893	Second symmetric 16.934/12.389	Third symmetric 22.000/20.155
Out-of plane	First symmetric 7.860/5.664	Second asymmetric 16.846/13.117	Third symmetric 24.023/21.988

Table 7. Comparison of ***measured/predicted*** eigen-frequencies for four stone-masonry bridges (***pinned*** boundary conditions).

Measured/predicted eigen-frequencies (Hz) for the ***Konitsa Bridge***			
In-plane	First asymmetric 5.176/6.733	Second symmetric 7.715/7.078	Third symmetric 12.549/10.085
Out-of plane	First symmetric 2.539/2.526	Second asymmetric 4.883/4.759	Third symmetric 7.129/7.706
Measured eigen-frequencies (Hz) for the ***Kokorou Bridge***			
In-plane	First asymmetric 7.275/10.212	Second symmetric 10.059/11.134	Third symmetric 17.139/15.125
Out-of plane	First symmetric 4.541/4.548	Second asymmetric 7.471/8.408	Third symmetric 10.303/13.733
Measured eigen-frequencies (Hz) for the ***Tsipiani Bridge***			
In-plane	First asymmetric 6.934/7.106	Second symmetric 8.549/10.029	Third symmetric 14.209/12.742
Out-of plane	First symmetric 3.320/3.321	Second asymmetric 6.348/6.257	Third symmetric 12.207/10.012
Measured eigen-frequencies (Hz) for the ***Kontodimou Bridge***			
In-plane	First Asymmetric 11.621/11.905	Second Symmetric 16.934/12.395	Third Symmetric 22.000/20.185
Out-of plane	First Symmetric 7.860/7.643	Second Asymmetric 16.846/17.035	Third Symmetric 24.023/26.362

Konitsa Bridge. Emasonry = 4000 MPa, Econtact = 2000 MPa. Bending Stiffness Modifiers = 3.0.
Kokorou Bridge. Emasonry = 4000 MPa, Econtact = 2000 MPa. Bending Stiffness Modifiers = 1.75.
Tsipianis Bridge. Emasonry = 4000 MPa, Econtact = 2000 MPa. Bending Stiffness Modifiers = 1.0.
Kontodimou Bridge. Emasonry = 1600 MPa, Econtact = 1600 MPa. Bending Stiffness Modifiers = 1.0.

Table 8. Comparison of ***measured/predicted*** eigen-frequencies for four stone-masonry bridges (***fixed*** boundary conditions).

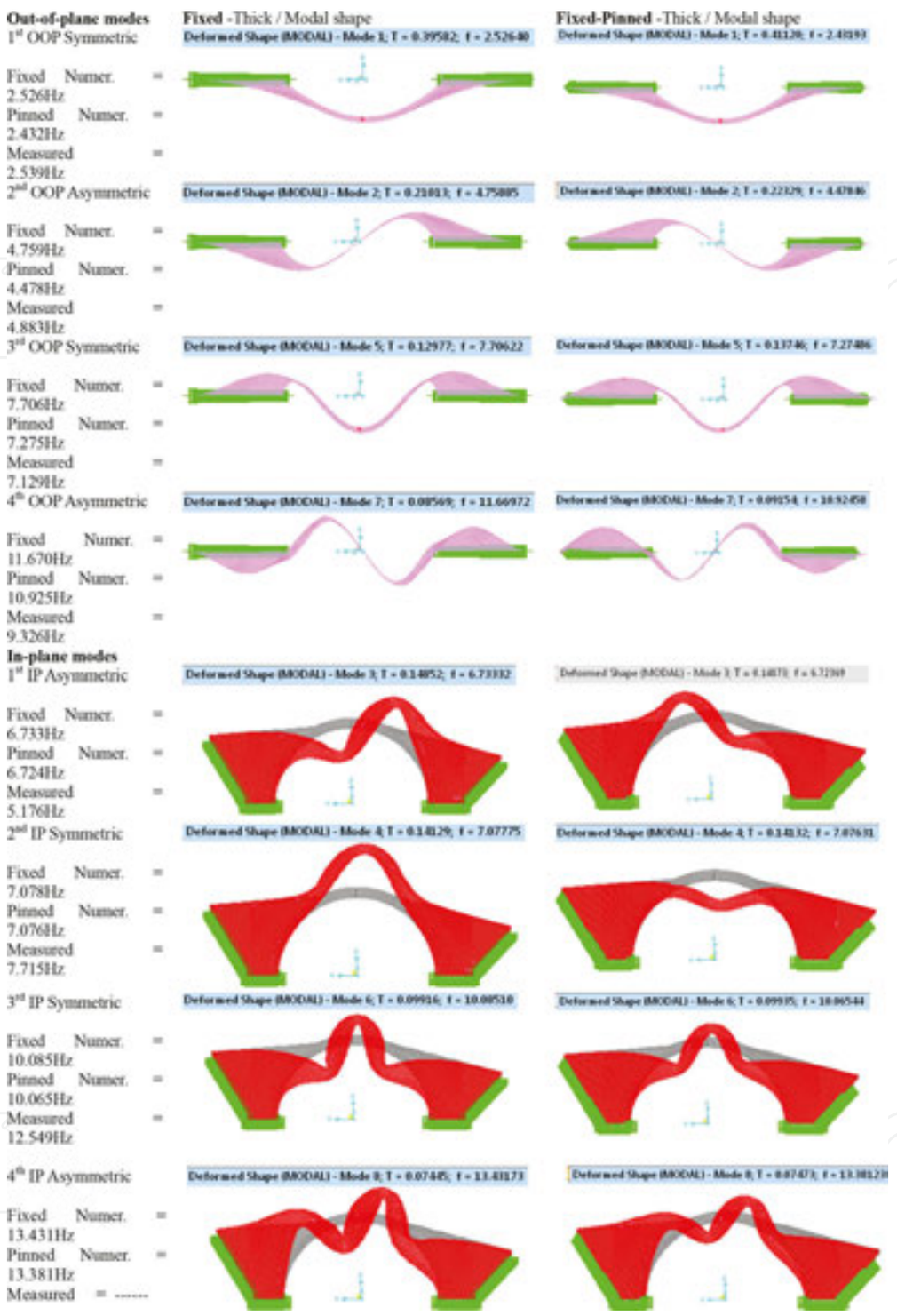

Figure 24. Numerical and observed eigen-values for the ***Konitsa Bridge***. $E_{masonry}$ =4000MPa, $E_{contact}$ =2000MPa. Bending Stiffness Modifiers = 3.0.

The approximation adopted in this study is a process of back simulation [6, 7]. That is, adopting values for these unknown mechanical stone-masonry properties, respecting at the same time all the measured geometric details, which result in reasonably good agreement between the

http://dx.doi.org/10.5772/64752

measured and predicted in this way eigen-frequency values. Following this approximate process, two distinct cases of boundary conditions were introduced. In one series of numerical simulations, all the boundaries, either at the river bed or at the river banks, were considered as being fixed in these 3-D numerical simulations for all studied bridges. This is denoted in the predicted eigen-frequency values in **Tables 7** and **8** and **Figures 24** and **25** with the subscript '*Fixed Numer*'. Alternatively, the rotational degrees of freedom were released all along the locations where the abutments are supported at the river banks thus excluding the footings. This is denoted in the predicted eigen-frequency values in **Tables 7** and **8** and **Figures 24** and **25** with the subscript '*Pinned Numer*'. It is shown from this sensitivity analysis that this variation in the boundary conditions approximation influences, as expected, the out-of-plane and not the in-plane stiffness of the studied stone-masonry bridges. This out-of-plane stiffness variation is more pronounced for the relatively small dimensions Kontodimou Bridge rather than for the relatively large Konitsa Bridge and Plaka Bridge. Moreover, for the Tsipianis Bridge

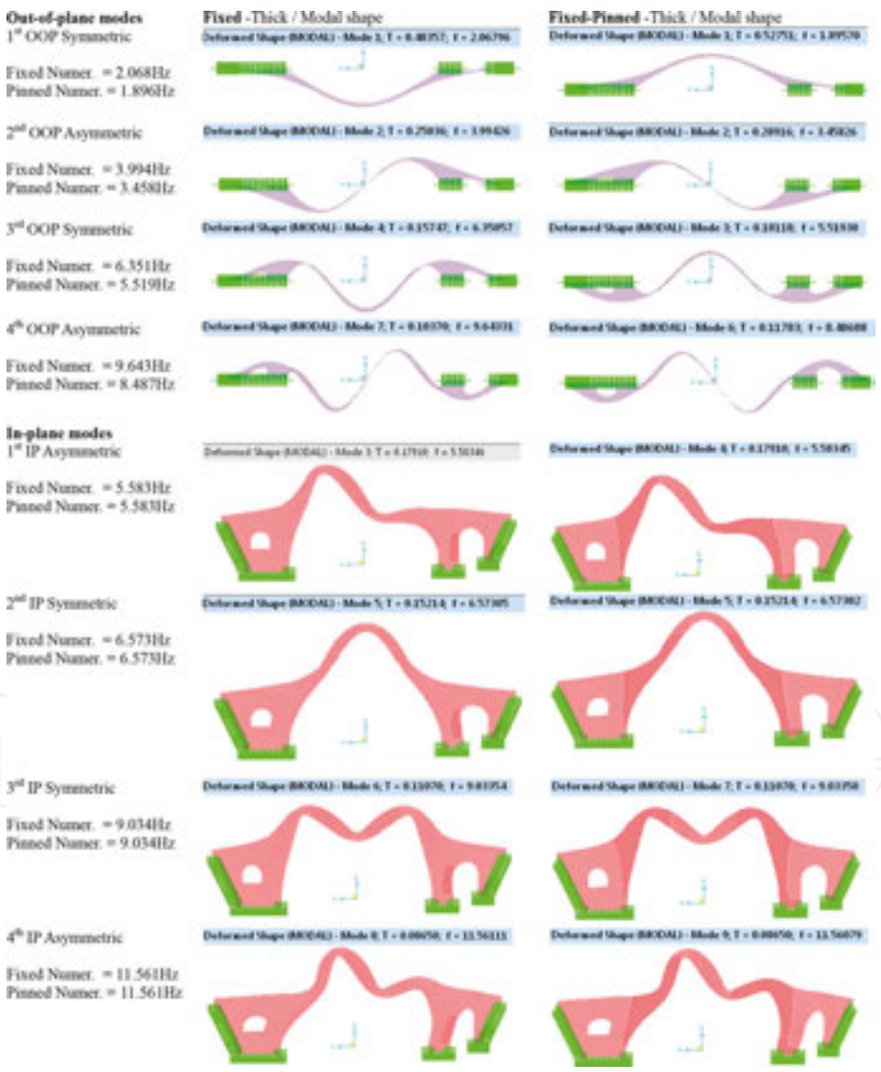

Figure 25. Numerical eigen-values for the Plaka Bridge. ***Plaka Bridge***. $E_{masonry}$ = 4000 MPa, $E_{contact}$ = 2000 MPa. Bending stiffness modifiers = 3.0.

whereby the main central arch is supported at the North end in adjacent arches rather than on the rocky bank, this variation of the boundary conditions, as expected, has again a less pronounced influence. The value of Young's modulus that was adopted for the masonry in these numerical simulations is listed at the bottom of **Table 8** and at the captions of **Figures 24** and **25** that depict the numerical eigen-mode and eigen-frequency numerical results together with the measured *in situ* eigen-frequency values for each bridge. Thus, for the Konitsa (**Figure 24**), Kokorou and Tsipianis Bridges, 4 GPa was adopted for the masonry Young's modulus and 2 GPa for the contact surface. For the Kontodimou Bridge, these values were 1.6 GPa for both the masonry and the contact surface. A partial explanation is that the mortar joints and contact surface between the various bridge parts in the Kontodimou Bridge (**Figure 10e** and **f**) were wider than in other bridges and the mortar was in some cases washed out at some depth. In order to approximate the in-plane and the out-of-plane stiffness of the studied stone-masonry bridges, which directly influences the corresponding numerical eigen-frequency values, listed in **Tables 7** and **8** and depicted in **Figures 24** and **25**, a flexural stiffness amplifier was introduced for the Konitsa Bridge and the Kokorou Bridge equal to 3.0 and 1.75, respectively. From the comparison of the results of these numerical simulations in terms of eigen-frequencies and eigen-modes, listed in **Tables 7** and **8** and depicted in **Figures 24** and **25**, it can be seen that in most cases the predicted eigen-frequency values are in reasonably good agreement with the measured values. Moreover, the order of the out-of-plane and the in-plane eigen-modes predicted by the numerical simulation is in agreement with the observed response. An exception is the first asymmetric in-plane eigen-mode for the Konitsa Bridge (**Figure 24**) and Kokorou Bridge (**Tables 7** and **8**) that indicates a corresponding measured stiffness smaller than the predicted one. On the basis of this comparison, an additional numerical simulation was performed for the Plaka Bridge (**Figure 25**), despite the lack of measured response in this case, adopting the same assumptions that were described before specifically for the Konitsa Bridge. As can be seen by comparing the numerical eigen-frequency values of the Konitsa Bridge (**Figure 24**) with those of the Plaka Bridge (**Figure 25**), the latter, as expected, is more flexible both in the in-plane and in the out-of-plane direction.

7. Simplified numerical investigation of the seismic behaviour of the studied stone-masonry bridges

7.1. Simplified dynamic spectral numerical simulation of the seismic behaviour of the Konitsa Bridge

This section includes results of a series of numerical simulations of the Konitsa Bridge when it is subjected to a combination of actions that include the dead weight (D) combined with seismic forces. The seismic forces will be defined in various ways, as will be described in what follows. Initially, use is made of the current definition of the seismic forces by EURO-Code 8 [12]. Towards this, horizontal and vertical design spectral curves are derived based on the horizontal design ground acceleration. This value, as defined by the zoning map of the current Seismic Code of Greece [13, 14], is equal to 0.16 g (g is the acceleration of gravity) for the location

http://dx.doi.org/10.5772/64752

of the Konitsa Bridge. Furthermore, it is assumed that the soil conditions belong to category A because of the rocky site where this bridge is founded, that the importance and foundation coefficients have values equal to one (1.0); the damping ratio is considered equal to 5% and the behaviour factor is equal to 1.5 (unreinforced masonry). The design acceleration spectral curves obtained in this way are depicted in **Figure 26a** and **b** for the horizontal and vertical direction, respectively. In the same figures, the corresponding elastic acceleration spectral curves are also shown derived from the ground acceleration recorded during the main event of the earthquake sequence of 5 August 1996 at the city of Konitsa located at a distance of approximately 1.5 km from the site of the bridge [15]. In **Figure 26a** and **b**, the eigen-period range of the first 12 eigen-modes is also indicated (ranging between the low and the high modal period). For the vertical response spectra, this is done for only the in-plane eigen-modes (see also **Table 9**).

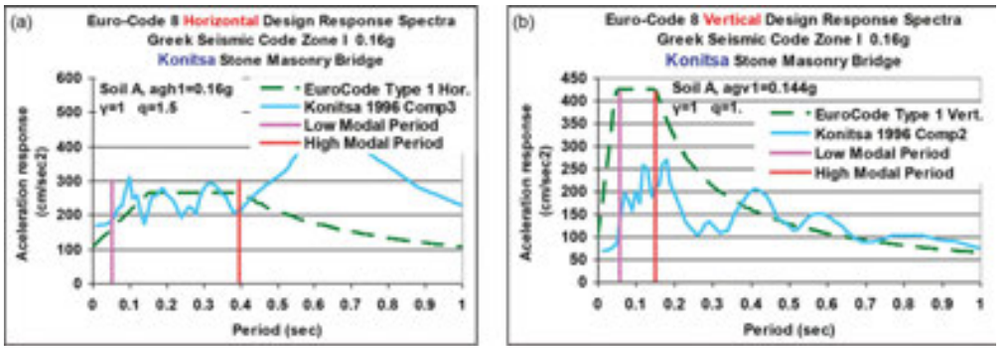

Figure 26. (a) Horizontal spectral curves for the 1996-Konitsa earthquake and the type-1 Euro-Code and (b) vertical spectral curves for the 1996-Konitsa earthquake and the type-1 Euro-Code.

As can be seen in **Figure 26a**, the Euro-Code horizontal acceleration spectral curves compare well with the horizontal component-3 of 1996 Earthquake spectral curves for the period range of interest. The Euro-Code vertical acceleration spectral curves, depicted in **Figure 26b**, are approximately 100% larger than the vertical component-2 of 1996 Earthquake spectral curves for the period range of interest. Based on these plots, it can be concluded that this bridge sustained a ground motion that in the horizontal direction was approximately comparable to the design earthquake; however, the design earthquake in the vertical direction is shown to be more severe than the one this stone-masonry bridge experienced during the 1996 earthquake sequence.

In **Table 10**, the base reactions are listed (F_X, F_Y and F_Z) in the x-x ($u1$, out-of-plane), the y-y ($u2$, in-plane) and z-z ($u3$, in-plane) directions (see **Figure 15a** and **b**) from the various load cases, which were considered in this numerical study. Apart from the dead load (D, row 1) in rows 2–4 of **Table 10**, the base reaction values listed are obtained from dynamic spectral analyses employing the horizontal and vertical response spectral curves of the 1996-Konitsa earthquake event (**Figure 26a** and **b**). In rows 7–9 of **Table 10**, the base reaction values are again obtained from dynamic spectral analyses employing this time the Euro-Code horizontal and vertical design spectral curves of **Figure 26a** and **b**. In all these dynamic spectral analyses, the 12 eigen-modes listed in **Table 9** were employed.

Output case Text	Period s	Frequency Hz	U_X Unitless	U_Y Unitless	U_Z Unitless	SumU_X Unitless	SumU_Y Unitless	SumU_Z Unitless
Mode 1 (first OOP Symmetric)	0.396	2.5264	0.3300	0	0	0.33002	0	0
Mode 2 (second OOP asymmetric)	0.210	4.7588	0.0004	0	0	0.33043	0	0
Mode 3 (first IP asymmetric)	0.149	6.7333	0.0	0.08498	0.00055	0.33043	0.08498	0.00055
Mode 4 (second IP symmetric)	0.141	7.0777	0.0	0.00104	0.12769	0.33043	0.08602	0.12825
Mode 5 (third OOP symmetric)	0.130	7.7062	0.2271	0	0	0.55753	0.08602	0.12825
Mode 6 (third IP symmetric)	0.099	10.0851	0.0	0.0007	0.15393	0.55753	0.08672	0.28218
Mode 7 (fourth OOP asymmetric)	0.086	11.6697	0.0	0	0	0.55754	0.08672	0.28218
Mode 8 (fourth IP asymmetric)	0.074	13.4317	0.0	0.17916	0.0023	0.55754	0.26588	0.28447
Mode 9 (fifth OOP symmetric)	0.065	15.2999	0.08851	0	0	0.64605	0.26588	0.28447
Mode 10 (fifth IP symmetric)	0.062	16.0400	0.0	0.23382	0.000014	0.64605	0.49971	0.28449
Mode 11 (sixth IP asymmetric)	0.0565	17.6794	0.0	0.0026	0.08175	0.64605	0.5023	0.36624
Mode 12 (sixth OOP asymmetric)	0.0522	19.1439	0.00262	0	0	0.64868	0.5023	0.36624

Table 9. Modal participating mass ratios for Konitsa Bridge (see **Figure 24**).

As can be seen in **Table 9**, these eigen-modes have modal mass participation ratios that result in sums smaller than 90%. That is, SumU_x = 64.9%, SumU_y = 50.2% and SumU_z = 36.6% of the total mass for the direction of motion in the U_x, U_y and U_z axes, respectively. This was accounted for in the subsequent load combinations where the dead load is combined with the horizontal and vertical spectral curves (rows 5 and 6 of **Table 10**, Combination 1, 1996 earthquake horizontal + vertical spectral curves and rows 10 and 11 of **Table 10**, Combination 7 Euro-Code horizontal + vertical spectral curves). Towards this end, the dynamic spectral analysis results were multiplied by an amplification factor equal to the reverse of the relevant ratio values before superimposing the dead load results. This amplification factor is equal to 1/SumU_x for

http://dx.doi.org/10.5772/64752

the dynamic analyses employing the out-of-plane *x*-*x* horizontal eigen-modal ratio, to 1/SumU_y for the in-plane *y*-*y* horizontal eigen-modal ratios and to 1/SumU_z for the in-plane vertical eigen-modal ratios [11]. This becomes evident when one compares the base reaction values without and with these amplification factor values in **Table 10**.

	Loading case description	Loading type description	Type limit	Global F_X (kN)	Global F_Y (kN)	Global F_Z (kN)
1	DEAD (D)	Linear Static		0	0	35,853
2	1996 Comp 2 RS Ver IP	Linear Resp. Spectral 1996 EQ	Max	0	179	1499
3	1996 Comp 3 RS Hor *u*1 OP	Linear Resp. Spectral 1996 EQ	Max	3130	0	0
4	1996 Comp 3 RS Hor *u*2 IP	Linear Resp. Spectral 1996 EQ	Max	0	2552	230
5	Combination 1	Dead + 1996 EQ RS (*u*1+ *u*2 + *u*3)	Max	4825	5574	40,406
6	Combination 1	Dead + 1996 EQ RS (*u*1+ *u*2 + *u*3)	Min	−4825	−5574	31,299
7	Euro-Code RS Hor *u*1 OP	Linear Resp. Spectral Euro-Code	Max	3725	0	0
8	Euro-Code RS Hor *u*2 IP	Linear Resp. Spectral Euro-Code	Max	0	2224	193
9	Euro-Code RS Ver *u*3 IP	Linear Resp. Spectral Euro-Code	Max	0	443	3426
10	Combination 7	Dead + Euro-Code RS (*u*1+ *u*2 + *u*3)	Max	5742	5640	45,597
11	Combination 7	Dead + Euro-Code RS (*u*1+ *u*2 + *u*3)	Min	−5742	−5640	26,109

Table 10. Base reactions from the dynamic spectral analyses, Konitsa Bridge.

In **Figure 27a** and **b**, the numerically predicted deformation patterns of Konitsa Bridge are depicted for load combination 1 and 7, respectively. As can be seen, this stone-masonry bridge develops under these combinations of dead load and seismic forces relatively large out-of-plane displacements at the top of the main arch. As expected, the deformations for the Euro-Code design spectra reach the largest values attaining at the crown of the arch a maximum value equal to 30.6 mm. In **Figure 28a–h**, the numerically predicted state of stress (max/min S11, max/min S22), which develops at Konitsa Bridge for load combinations 1 and 7, is depicted. Again, as expected, the most demanding state of stress results for the load combination 7 that includes seismic forces provided by Euro-Code [12]. The largest values of tensile stress S11 (3.46 MPa, **Figure 28b**) develop at the bottom fibre of the crown of the arch. This is a relatively large tensile stress value that is expected to exceed the tensile capacity of the stone masonry of this bridge [16]. The largest value of tensile stress S22 (1.5 1 MPa, **Figure 28f**) develops at the area where the primary arch joins the foundation block. Again, this is a relatively large tensile stress value that is expected to exceed the tensile capacity of the stone masonry of this bridge. Both these remarks indicate locations of distress for this stone-masonry bridge predicting in this way the appearance of structural damage. On the contrary, the largest value of compression stress equal to S11 = −4.3 MPa (**Figure 28d**, for combination 7) is expected to be easily met by the compression capacity of the stone masonry for this bridge [16].

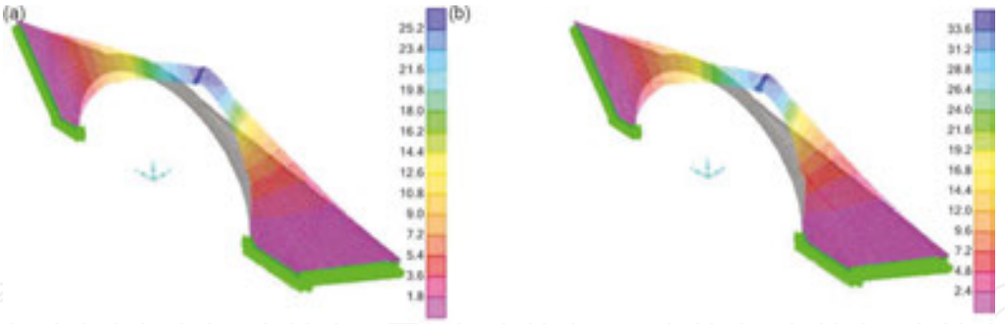

Figure 27. (a) Deformations of Konitsa Bridge. For loads Dead + 1996 EQ RS ($u1$+ $u2$ + $u3$). Comb 1. At crown $u1$ = 24.643 mm, $u2$ = 1.209 mm, $u3$ = −10.593 mm. (b) Deformations of Konitsa Bridge. For loads Dead + Euro-Code RS ($u1$+ $u2$ + $u3$). Comb 7. At crown $u1$ = 30.573 mm, $u2$ = 1.348 mm, $u3$ = −15.804 mm.

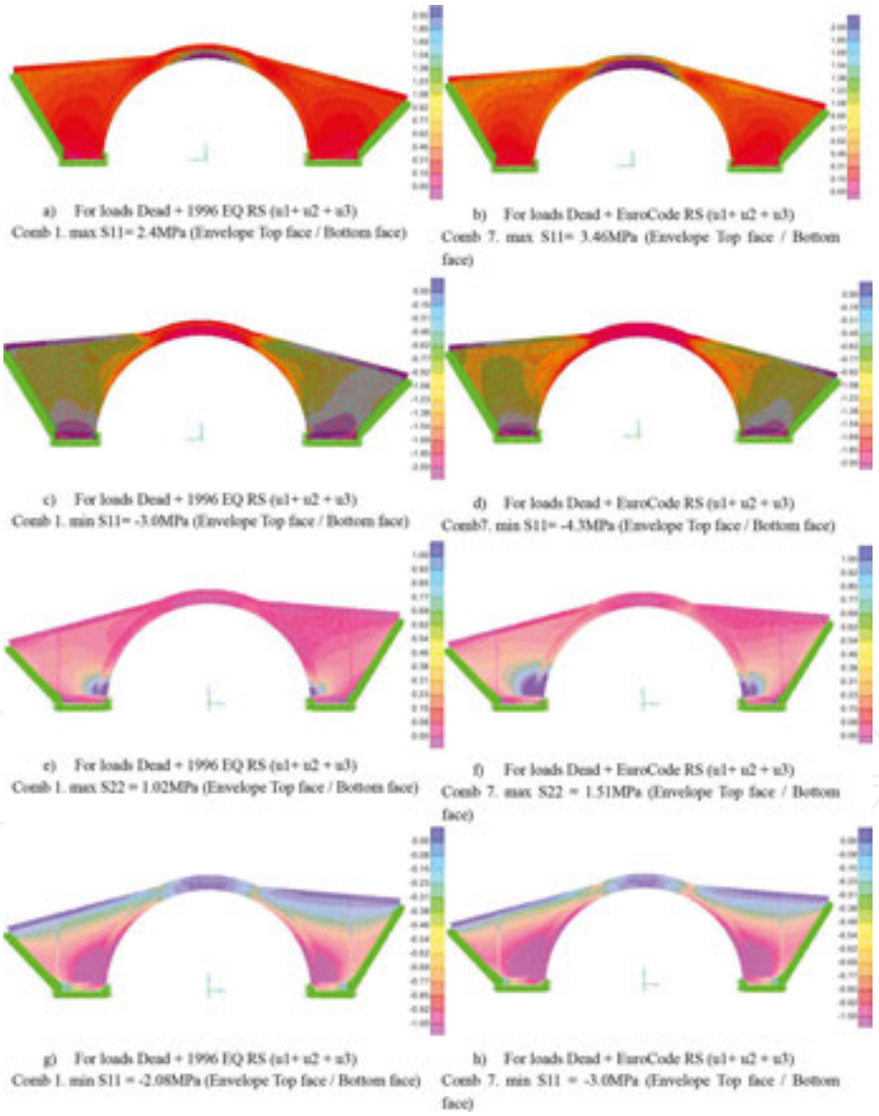

Figure 28. State of stress through the distribution of stresses S11 and S22 for Konitsa Bridge.

http://dx.doi.org/10.5772/64752

7.2. Dynamic elastic time-history numerical simulation of the seismic behaviour of the Konitsa Bridge

An additional linear numerical simulation was performed. This time, apart from the dead load (D, row 1, **Table 11**), the Konitsa Bridge was subjected to the horizontal component (Comp3) and/or the vertical component [17] of the 1996-Konitsa earthquake record (**Figure 29**) in the following way. The bridge was subjected only to the vertical (Comp2-Ez, rows 2 and 3 of **Table 11**) or only to the horizontal component of this record in the out of-plane direction (Comp3-Ex, rows 4 and 5 of **Table 11**). Alternatively, the bridge was subjected to the horizontal component of this record in the in-plane horizontal direction (Comp3-Ey, rows 6 and 7, **Table 11**) [15].

The solution this time was obtained through a step-by-step time integration scheme assuming a damping ratio equal to 5% of critical. In these analyses, only the first most intense 6 s of this 1996-Konitsa earthquake record were used [15]. In **Table 11**, the base shear values in the *x*-*x* (F_X, $u1$, horizontal out-of-plane), *y*-*y* (F_Y, $u2$, horizontal in-plane) and *z*-*z* (F_Z, $u3$, vertical) directions are listed in terms of limit values (maximum or minimum) that arose during the 6 s of these time-history analyses. Limit (maximum or minimum) base shear F_X, F_Y, F_Z values are also listed in rows 8–13 when these seismic excitations (Ex, Ey and Ez) are combined within themselves and the dead load as is shown in the third column of **Table 11** to produce load combinations encoded as COMB9, COMB10 and COMB11. By comparing these base shear values with the ones listed in **Table 10** where the response spectral curves of either the 1996-Konitsa record or the Euro-Code were employed, it can be seen that the limit (max/min) base shear amplitudes in both tables are very similar. **Figure 30a** shows the horizontal (u_x, out-of-plane) and the vertical (u_z, in-plane) displacement response at the crown of the Konitsa Bridge, obtained from the time-history numerical analyses. The horizontal response was obtained when the structure was subjected to horizontal component (Comp3) of the Konitsa 1996 earthquake record and the vertical in-plane response when the structure is subjected to vertical component (Comp2) of the Konitsa 1996 earthquake record (**Figure 29**). **Figure 30b** shows the variation of the S11 stress response at the bottom fibre of the crown of the Konitsa Bridge when this structure is subjected to either the horizontal component of the Konitsa 1996 earthquake record (Comp3) in the out-of-plane (u_x) direction or the vertical component of the Konitsa 1996 earthquake record (Comp2) in the vertical (u_z) in-plane direction. The location of the plotted stress is at the bottom fibre at the middle of the arch (crown) of the Konitsa Bridge. As can be seen in both **Figure 30a** and **b**, the horizontal u_x displacement and S11 stress response produced by the horizontal out-of-plane excitation are larger than the corresponding response vertical u_z displacement and S11 stress response produced by the vertical in-plane excitation. Moreover, as expected from the relevant response spectral curves depicted and the dominant eigen-frequency values (**Figures 24**, **26a** and **b**), the vertical u_z displacement and S11 stress response, produced by the vertical in-plane excitation, are of higher frequency content than the horizontal u_x displacement and S11 stress response produced by the horizontal out-of-plane excitation.

	Loading case description	Loading type description	Type limit	Global F_X (kN)	Global F_Y (kN)	Global F_Z (kN)
1	DEAD	Dead Load (D) Linear Static		0	0	35,853
2	Comp 2 TH Ver *u*3 IP	Konitsa 1996 Comp 2 THist. Ver *u*3 In-Plane (Ez)	Max	0	128.6	2651.2
3	Comp 2 TH Ver *u*3 IP	Konitsa 1996 Comp 2 THist. Ver *u*3 In-Plane (Ez)	Min	0	−140.2	−2380.5
4	Comp 3 TH Hor *u*1 OP	Konitsa 1996 Comp 3 THist. Hor *u*1 Out-of-Plane (Ex)	Max	5254.6	0	0
5	Comp 3 TH Hor *u*1 OP	Konitsa 1996 Comp 3 THist. Hor *u*1 Out-of-Plane (Ex)	Min	−5786.6	0	0
6	Comp 3 TH Hor *u*2 IP	Konitsa 1996 Comp 3 THist. Hor *u*2 In-Plane (Ey)	Max	0	4608.7	88.2
7	Comp 3 TH Hor *u*2 IP	Konitsa 1996 Comp 3 THist. Hor *u*2 In-Plane (Ey)	Min	0	−6456.7	−81.9
8	COMB9	Dead + Ex + Ez	Max	5254.6	128.6	38,504.2
9	COMB9	Dead + Ex + Ez	Min	−5786.6	−140.2	33,472.5
10	COMB10	Dead + Ey + Ez	Max	0	4737.3	38,592.4
11	COMB10	Dead + Ey + Ez	Min	0	-6596.9	33,390.7
12	COMB11	Dead + Ex + Ey + Ez	Max	5254.6	4737.3	38,592.4
13	COMB11	Dead + Ex + Ey + Ez	Min	−5786.6	−6596.9	33,390.7

Table 11. Base reactions from time-history analyses: Konitsa Bridge.

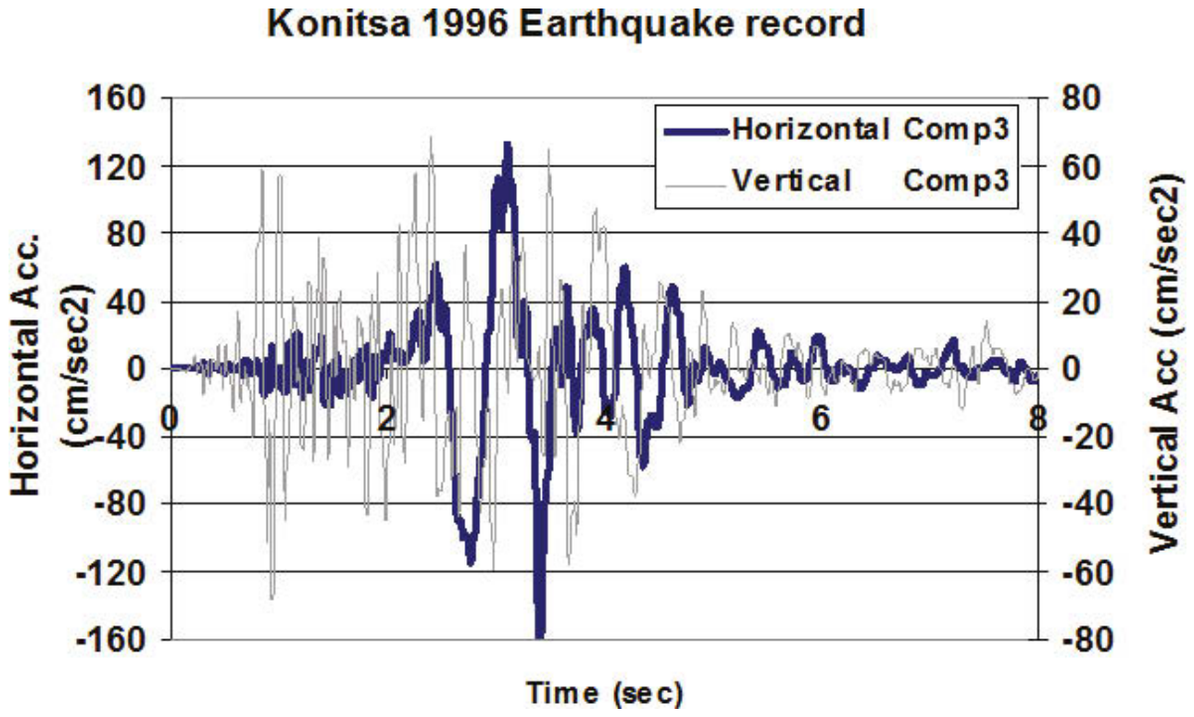

Figure 29. The first eight (8) most intense seconds of the 1996 earthquake record (ITSAK).

http://dx.doi.org/10.5772/64752

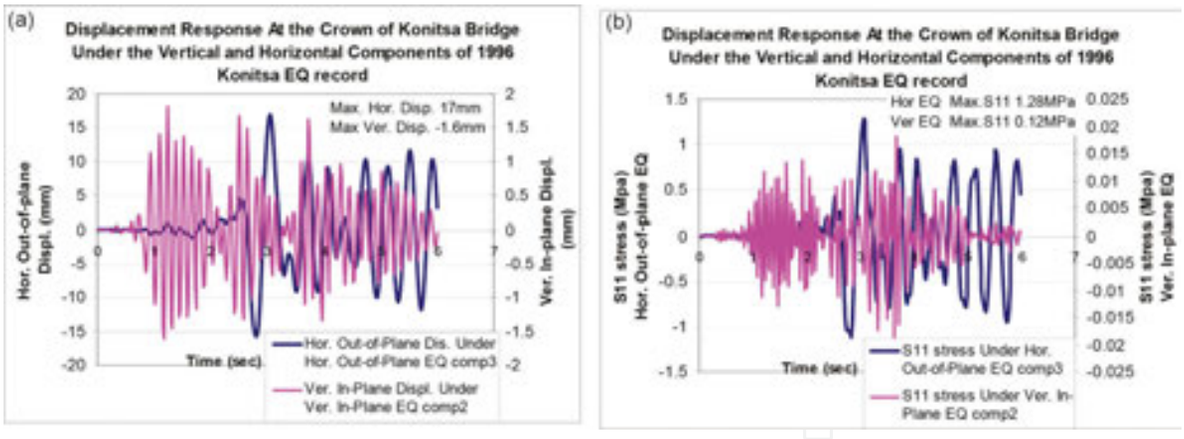

Figure 30. (a) Displacement (Hor. or Ver.) response at the crown of the Konitsa Bridge when subjected to either the horizontal or the vertical component of the Konitsa 1996 earthquake. (b) S11 stress response at the bottom of crown of the Konitsa Bridge when subjected to either the horizontal or the vertical component of the Konitsa 1996 earthquake.

Figure 31a and **b** depict the envelop of the limit (maximum/minimum) values of the S11 stress distribution in the Konitsa Bridge for load combination 11 that includes the dead load, the application of Comp3 of the Konitsa earthquake record in both the horizontal in-plane and out-of-plane direction as well as Comp2 of the Konitsa earthquake record in the vertical in-plane direction. By examining the displacement and stress response, it could be concluded that the application of the horizontal component of the Konitsa 1996 in the horizontal u_y in-plane direction is of too small amplitude to be of any significance. This must be attributed to the stiffness properties of this bridge in this direction and the resulting in-plane eigen-frequencies and eigen-modes that combined with the frequency content of this record result in displacement and stress response of relatively small amplitude. By comparing these S11 stress response maximum/minimum values with the ones shown in **Figure 28** where the response spectral curves of either the 1996-Konitsa record or the Euro-Code were employed (Section 7.1.), it can be seen that the limit (max/min) S11 stress maximum/minimum amplitudes is very similar, as expected, to the corresponding values obtained from the dynamic spectral analyses employing the 1996-Konitsa record spectral curves. As was discussed before, the Euro-Code design

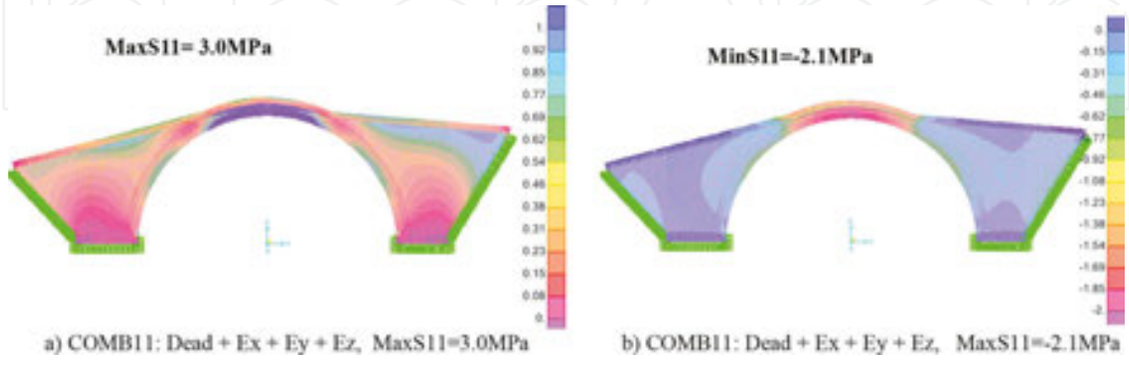

Figure 31. State of stress through the distribution of stresses S11 (envelope) at the bottom fibre of the crown for Konitsa Bridge.

spectral curves result in much higher displacement and stress demands for the Konitsa Bridge. From all these numerical analyses, it can be concluded that the most vulnerable part of this stone-masonry bridge is the slender central part of the main arch, composed as described in Section 3 of the primary and secondary arch, when the structure is subjected to seismic forces in the horizontal out-of-plane direction. The vertical in-plane excitation is expected to be significant when in-phase with the horizontal excitation in a way that it can offset the beneficial effect of the dead weight. This observation is thought to be of a general nature, as it is demonstrated by the numerical analyses of the Plaka Bridge in the following Section 7.3.

7.3. Simplified numerical simulation of the seismic behaviour of the Plaka Bridge

This section includes results of a series of numerical simulations of the Plaka Bridge when it is subjected to a combination of actions that include the dead weight (D) combined with seismic forces. The seismic forces will be defined as was done in Section 7.1 by making use of the current definition of the seismic forces by EURO-Code 8 [12]. Towards this, horizontal and vertical design spectral curves are derived based on the horizontal design ground acceleration. This value, as it is defined by the zoning map of the current Seismic Code of Greece, is equal to 0.24 g (g is the acceleration of gravity) for the location of the Plaka Bridge [13, 14]. Furthermore, it is assumed that the soil conditions belong to category A because of the rocky site where this bridge is founded, that the importance and foundation coefficients have values equal to one (1.0), the damping ratio is considered equal to 5% and the behaviour factor is equal to 1.5 (unreinforced masonry). The design acceleration spectral curves obtained in this way are depicted in **Figure 32a** and **b** for the horizontal and vertical direction, respectively. In **Figure 32a** and **b**, the eigen-period range of the first 12 eigen-modes is also indicated (ranging between the low and the high modal period). For the vertical response spectra, this is done for only the in-plane eigen-modes (see also **Table 11**). By comparing these design spectral acceleration curves (of **Figure 32a** and **b**) for the Plaka Bridge with the corresponding spectral curves for the Konitsa Bridge (**Figure 26a** and **b**), it becomes apparent that the former represent a more demanding seismic force level than the latter.

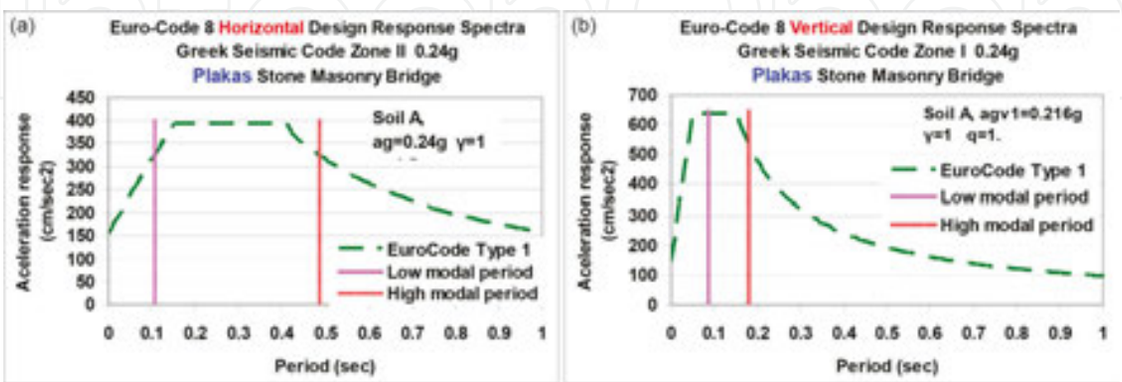

Figure 32. (a) Horizontal spectral curves for type-1 Euro-Code to be applied in Plaka bridge and (b) vertical spectral curves for type-1 Euro-Code to be applied in Plaka bridge.

http://dx.doi.org/10.5772/64752

For the Plaka Bridge, the modal mass participation ratios and the base reactions are listed in **Tables 12** and **13**, respectively. The base reactions are F_X, in the *x*-*x* (*u*1, out-of-plane), F_Y the *y*-*y* (*u*2, in-plane) and F_Z in the *z*-*z* (*u*3, in-plane) directions (see **Figures 7d**, **25**, **29a** and **b**) Apart from the dead load (D, row 1) in rows 2–4 of **Table 13**, the base reaction values were again obtained from dynamic spectral analyses employing, as was done in Section 7.1., the Euro-Code horizontal and vertical design spectral curves of **Figure 32a** and **b**. In all these dynamic spectral analyses, the 12 eigen-modes listed in **Table 12** were again employed. As can be seen in **Table 12**, these eigen-modes have modal mass participation ratios that result in sums that are SumU_x = 67.4%, SumU_y = 58.7% and SumU_z = 39.3% of the total mass for the direction of motion in the U_x, U_y and U_z axes, respectively. In the subsequent load combination 1, where the dead load is combined with the Euro-Code horizontal + vertical spectral curves, the dynamic spectral analysis results were multiplied again by an amplification factor equal to the reverse of the relevant ratio values before superimposing the dead load results. This amplification factor is equal to 1/SumU_x for the dynamic analyses employing the out-of-plane *x*-*x* horizontal eigen-modal ratio, to 1/SumU_y for the in-plane *y*-*y* horizontal eigen-modal ratios and to 1/SumU_z for the in-plane vertical eigen-modal ratios [11]. This becomes evident when one compares the base reaction values without and with these amplification factor values in **Table 13**.

Output Case	**Period**	**Frequency**	U_X	U_Y	U_Z	SumU_X	SumU_Y	SumU_Z
Text	**s**	**Hz**	**Unitless**	**Unitless**	**Unitless**	**Unitless**	**Unitless**	**Unitless**
Mode 1 (first OOP symmetric)	0.484	2.068	0.33622	0	0	0.33622	0	0
Mode 2 (second OOP asymmetric)	0.250	3.994	0.00003	0	0	0.33625	0	0
Mode 3 (first IP asymmetric)	0.179	5.583	0	0.10253	0	0.33625	0.1025	0.000008
Mode 4 (third OOP symmetric)	0.157	6.351	0.24674	0	0	0.58298	0.10253	0.000008
Mode 5 (second IP symmetric)	0.152	6.573	0	0.00067	0.13444	0.58298	0.1032	0.13445
Mode 6 (third IP symmetric)	0.111	9.034	0	0	0.16089	0.58298	0.10323	0.29533
Mode 7 (fourth OOP asymmetric)	0.104	9.463	0.00006	0	0	0.58304	0.10323	0.29533
Mode 8 (fourth IP asymmetric)	0.0865	11.561	0	0.37475	0.00011	0.58304	0.47797	0.29545
Mode 10 (fifth IP symmetric)	0.0787	12.706	0	0.10353	0.00049	0.58304	0.5815	0.29594
Mode 9 (fifth OOP symmetric)	0.0772	12.953	0.0914	0	0	0.67444	0.5815	0.29594
Mode 11 (sixth IP asymmetric)	0.0687	14.556	0	0.00557	0.09697	0.67444	0.58708	0.39291
Mode 12 (sixth OOP asymmetric)	0.0609	16.420	0.00186	0	0	0.6763	0.58708	0.39291

Table 12. Modal participating mass ratios for Plaka Bridge (see **Figure 25**).

	Loading case description	Loading type description	Type limit	Global F_X (kN)	Global F_Y (kN)	Global F_Z (kN)
1	DEAD (D)	Linear Static		0	0	42,544
2	Euro-Code RS Hor $u1$ OP	Linear Resp. Spectral Euro-Code	Max	6382	0	0
3	Euro-Code RS Hor $u2$ IP	Linear Resp. Spectral Euro-Code	Max	0	5773	311
4	Euro-Code RS Ver $u3$ IP	Linear Resp. Spectral Euro-Code	Max	0	677	6581
5	Combination 1	Dead + Euro-Code RS ($u1$+ $u2$ + $u3$)	Max	9436	11,555	59,823
6	Combination 1	Dead + Euro-Code RS ($u1$+ $u2$ + $u3$)	Min	−9436	−11,555	25,265

Table 13. Base reactions, Plaka Bridge.

In **Figure 33a** and **b**, the numerically predicted deformation patterns of Plaka Bridge are depicted for load combination 1. As can be seen, this stone-masonry bridge develops under this combination of dead load and seismic forces relatively large out-of-plane displacements at the top of the main arch. As expected, the out-of-plane displacement response of the Plaka Bridge, when subjected to Euro-Code design spectra, reaches the largest value at the crown of the arch with a maximum value equal to 52.84 mm. This maximum out-of-plane value for the Plaka Bridge is almost twice as large as the corresponding value predicted numerically for the Konitsa Bridge.

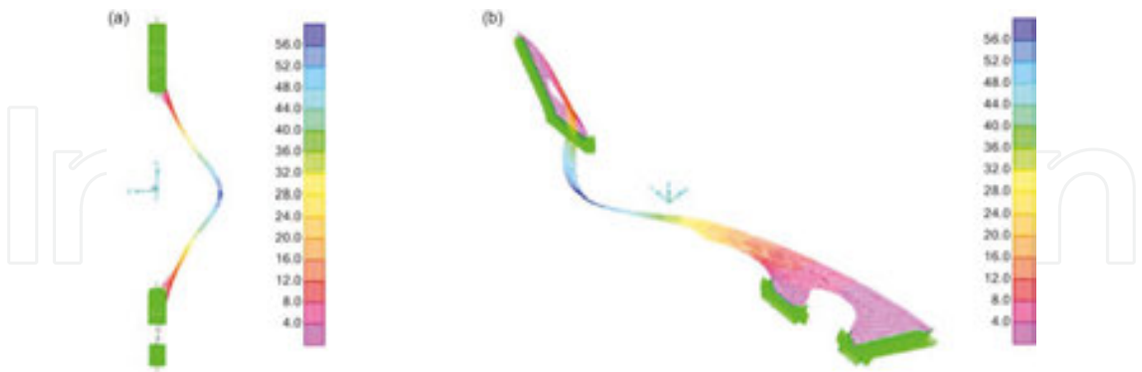

Figure 33. (a) Deformations of Plaka Bridge. For loads Dead + Euro-Code RS ($u1$+ $u2$ + $u3$). Comb 1. At crown $u1$ = −52.84 mm, $u2$ = −21.13 mm, $u3$ = −22.11 mm. (b) Deformations of Plaka Bridge. For loads Dead + Euro-Code RS ($u1$ + $u2$ + $u3$). Comb 1. At crown $u1$ = −52.84 mm, $u2$ = −21.13 mm, $u3$ = −22.11 mm.

In **Figure 34a–d**, the numerically predicted state of stress (max/min S11, max/min S22), which develops at Plaka Bridge for load combination 1, is depicted. Again, as expected, the most demanding state of stress results is for the load combination 1 that includes seismic forces

http://dx.doi.org/10.5772/64752

provided by Euro-Code. The largest value of tensile stress S11 (5.73 MPa, **Figure 34a**) develops at the bottom fibre of the crown of the arch. This relatively large tensile stress value [11, 16] is exceeding by far the tensile capacity of traditionally built stone masonry. The largest value of tensile stress S22 (3.40 MPa, **Figure 34c**) develops at the area where the toes of the primary arch join the foundation block. Again, this is a relatively large tensile stress value and is exceeding by far the tensile capacity of traditionally built stone masonry. Both these remarks indicate locations of distress for the Plaka stone-masonry bridge, as was done for the Konitsa Bridge predicting in this way the appearance of structural damage. On the contrary, the largest value of compressive stress equal to S11 = −6.14 MPa (**Figure 34d**, for combination 1) could be met by the compression capacity of the stone masonry for this bridge. The maximum tensile stress values that were numerically predicted for Plaka Bridge are approximately twice as large as the corresponding values obtained for Konitsa Bridge. This is due to the seismic forcing levels, which for Plaka Bridge are by 50% higher than those applied for Konitsa ridge. This is because Plaka Bridge is located in seismic zone II (design ground acceleration equal to 0.24 g) whereas Konitsa Bridge is located at seismic zone I (design ground acceleration equal to 0.16 g). Furthermore, although the main central arches of the two bridges are very similar in geometry (with the deck of the Plaka Bridge being somewhat wider than the deck of the Konitsa Bridge), the Plaka Bridge has a much larger total length than the Konitsa Bridge due to the construction of a mid-pier and arches adjacent to the main central arch. Thus, Plaka Bridge is more flexible and has a much larger total mass than the Konitsa Bridge. Based on these remarks, it is reasonable to expect for the Plaka Bridge larger seismic displacement values in the out-of-plane direction and consequently larger tensile stress values, than the corresponding values predicted for the Konitsa Bridge. The final consequence of these remarks is that, according to the

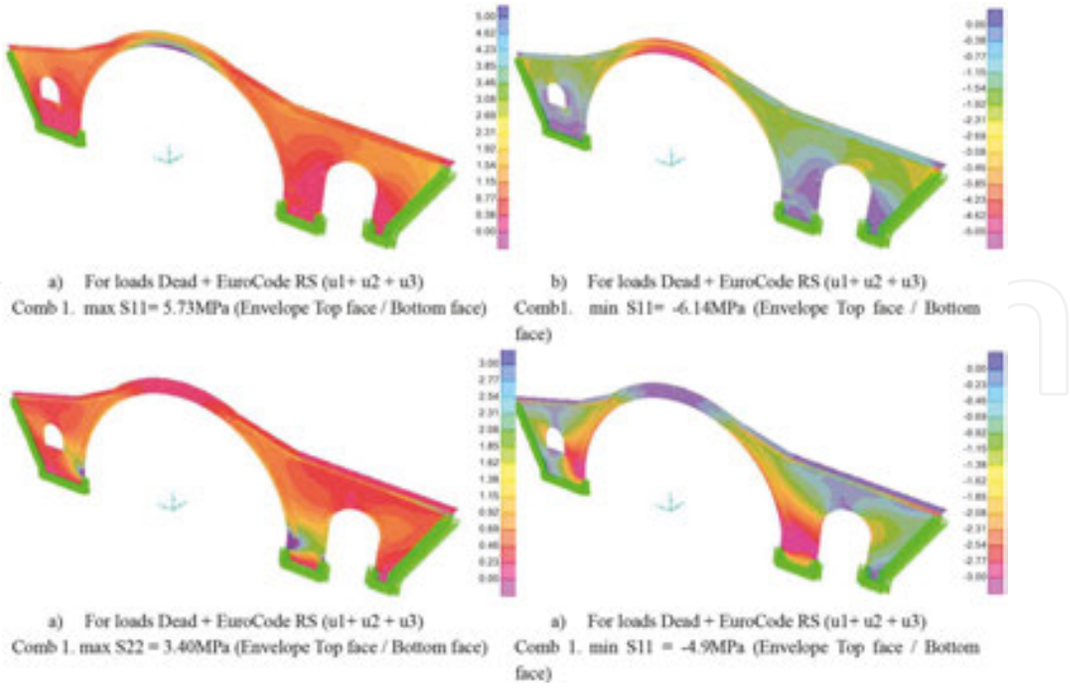

Figure 34. State of stress through the distribution of stresses S11 and S22 for Plaka Bridge.

results of this simplified numerical approach, the Plaka Bridge has a higher degree of seismic vulnerability than the Konitsa Bridge. A similar simplified numerical study of the performance of the Plaka Bridge could be done when measurements of flow data of the flooding of river Arachthos (31st January 2015) that caused the collapse of this bridge become available.

8. Non-linear numerical simulation of the seismic behaviour of the Konitsa stone-masonry bridge

A three-dimensional finite element model of the Konitsa stone bridge was developed and utilized in the linear (modal and gravity) and non-linear (earthquake) analyses [18, 19]. The general finite element software True-Grid (meshing) and LS-DYNA (static, modal, earthquake analyses) software were employed [20]. The developed three-dimensional model incorporated interface conditions between distinct parts of the structure (i.e. lower and upper stone arches, arches and abutments, etc.) in an effort to capture the interaction between the structural sections as well as differentiate between the building techniques and details that were introduced during the construction of the bridge and thus differentiate between the different failure criteria and mechanisms that may govern the different parts. A modelling approach where the elements (stones) of the arch are represented by solid elements with 'hybrid' behaviour was adopted and used throughout. The detailed model developed for this study included 4009 beam elements that formed the steel mesh in the intrados of the bridge rigidly connected to the stone array. The bridge was modelled using four different solid materials with 72,540 elements. As noted above, the different structural components are in 'contact' governed by contact interface conditions. The two arches have been modelled with solid 'hybrid' elements (stone-mortar behaviour) that capture the 'non-linearity' or failure rather than the pure contact between stones, an approach that is closer to the actual conditions in the structure. Specifically, it has been assumed that the 'hybrid' element representing mortar and stone behaves as one with the weakness attributed to the mortar part (Modulus and Poisson ratio represent the entire element but critical stresses are dependent on mortar).

The model is assumed to be fixed on competent rock on both sides and no soil-structure interaction (SSI) effects are considered. **Figure 35a** and **b** depict the finite element model that was developed and utilized based on *in situ* technical information collection, images and other historically available technical data. In developing the finite element method (FEM) model, special attention to the foundation and abutment details was paid and incorporated. Based on experience and data for similar structures, the first attempt in establishing the static and dynamic (modal) behaviour of the Konitsa Bridge utilized isotropic material properties for the mortar-stone material with Young's modulus E = 17 GPa, compressive strength of 30 MPa, Poisson's ratio of 0.21 and density of 2.69 g/cc. Orthotropic elastic behaviour of the hybrid stone-mortar material was also utilized in the numerical modal analysis during the calibration phase and following the field vibration test. This is described in [20] as one of the options for elastic materials but with orthotropic behaviour. **Figure 36a** depicts modelling details of the foundation of the Konitsa Bridge and of the way the primary and secondary arches are joined

http://dx.doi.org/10.5772/64752

with the foundation block. **Figure 36b** depicts the modelling detail of the parapet and the deck of the Konitsa Bridge (see also **Figure 20**).

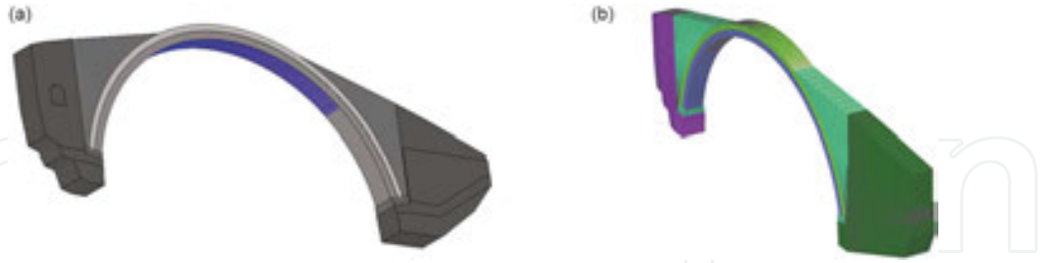

Figure 35. (a) Depiction of sections considered in modelling: the Konitsa stone arch bridge including the partial steel mesh over the intrados placed during restoration work prior to 1996 earthquake and (b) finite element model and details of Konitsa stone bridge.

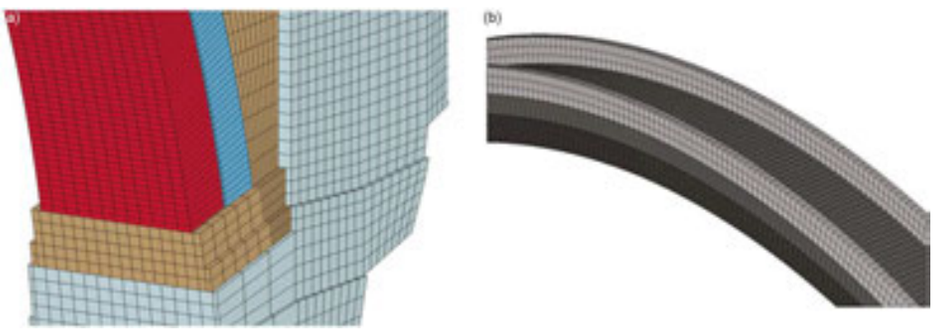

Figure 36. (a) Konitsa Bridge RHS foundation modelling details and (b) Konitsa Bridge parapet modelling details.

8.1. Modal and static analyses

Before proceeding to the complex non-linear analyses, a modal analysis was performed as a first attempt utilizing the numerical model depicted in **Figure 36a** and **b**. This was done using isotropic elastic material behaviour throughout the numerical model with material properties ρ = 2.69 g/cc, E = 17 GPa, ν = 0.21 for the two arches and similar values for the abutment and mandrel walls. The same process was followed, described in the numerical simulation of Section 6, whereby the measured eigen-frequencies, reported for this bridge in Section 4, were taken into account in the best possible way. This modal analysis led to mode and corresponding frequencies shown in **Figure 37**. The first five (5) modes include the first two bending modes, the first torsional mode, the first asymmetric vertical mode and the first pure vertical mode, as were also reported in Section 6. In what follows is again a comparison of the modal characteristics of the current 3-D numerical simulation with the results of the 3-D numerical simulation of Section 6 as well as with measured values. As can be seen from this comparison, the values of the eigen-frequencies for the out-of-plane eigen-modes compare well with the measured values, as was also discussed in Section 3. Moreover, as was also discussed in Section 6, certain discrepancies can be seen for the in-plane eigen-modes. It is believed that the use of

orthotropic properties for the materials employed in both the linear numerical simulations can correct up to a point these discrepancies.

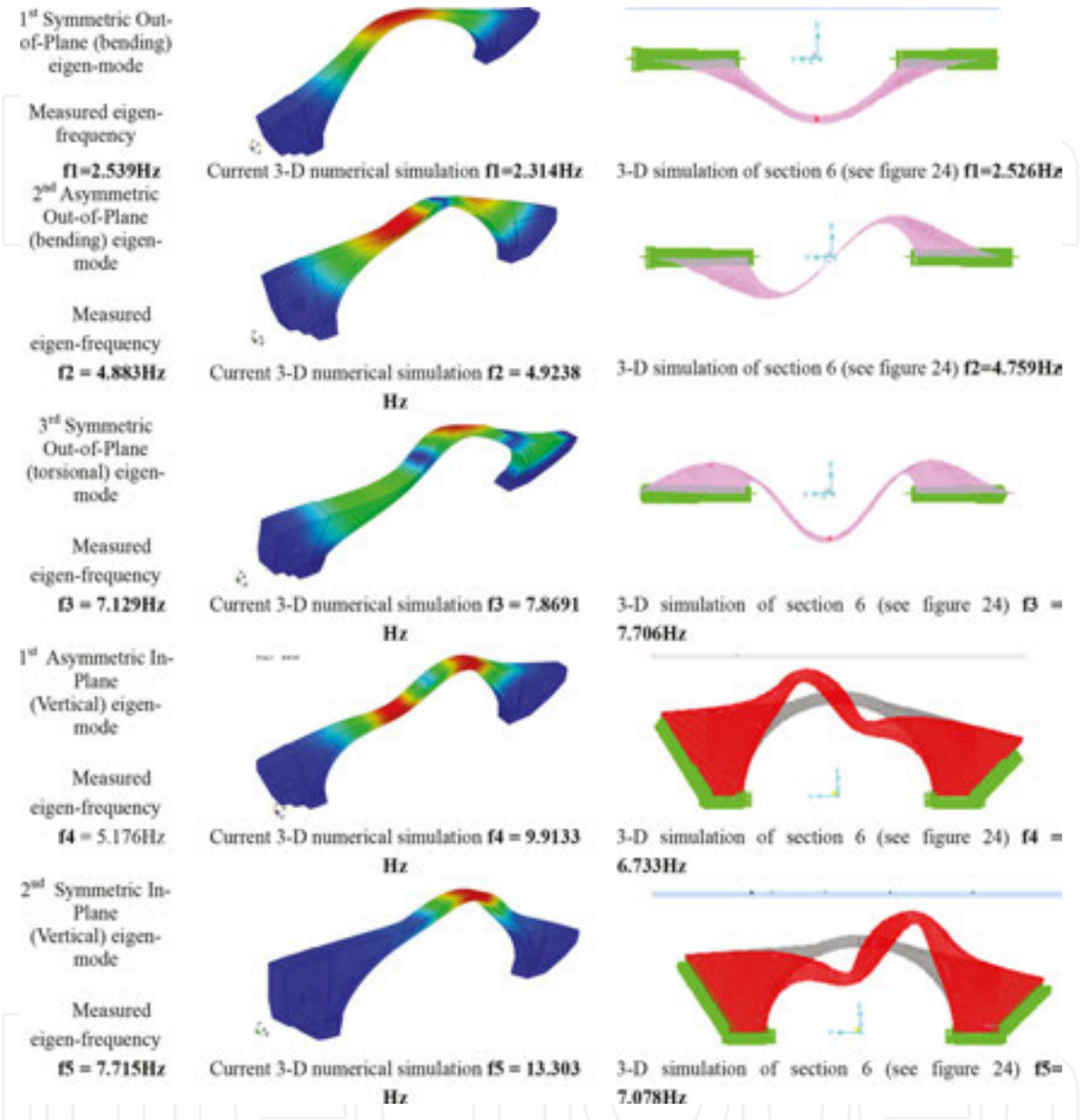

Figure 37. Comparison between numerically predicted eigen-frequencies with measured values.

8.2. Non-linear earthquake analysis and damage criteria

For the static analysis and subsequently dynamic (earthquake) analyses where the bridge structure is expected to exhibit non-linear behaviour and damage, the following material behaviour was adopted in this study.

The mortar-stone material was assumed to behave like 'pseudo-concrete' according to the Winfrith model. It is controlled by compressive and tensile strength as well as fracture energy and aggregate size.

http://dx.doi.org/10.5772/64752

The compressive strength is considered to be controlled by the stone portion of the hybrid element (30 MPa) and the tensile strength by that of the mortar. The range of the tensile strength assumed in this study for the different sections of the Konitsa Bridge is 0.25–2.1 MPa. The fracture energy assumed in the analysis dissipated in the opening of a tension crack assumed as 80 N/m. Upon formation of a tension crack, no tensile load can be transferred across the crack faces.

An additional failure criterion that controls the detachment of elements from the structure is that of pressure (negative in tension). This criterion is used to simulate the failure of mortar in the hybrid element, which is considered to fail when the negative pressure exceeds a critical value. The pressure threshold assumed in the study was 1.1 MPa.

8.3. Seismic analysis of the Konitsa Bridge

The most recent earthquake in the proximity of the Konitsa Bridge occurred in August 1996 [21]. The epicentre of the 6th August earthquake (M = 5.7) with 8-km depth was about 15 km to the South West (SW) of the bridge. While no recording at the bridge location is available, the earthquake was recorded at less than a kilometre away on soft soil with maximum acceleration of 0.39 g [22]. A similar recording on rock (~1 km away and on the same rock formation to that supporting the left-hand side (LHS) buttress of the Konitsa Bridge) indicated a peak ground acceleration of 0.19 g. During the 1996 earthquake, limited damage was experienced by the bridge in the form of (a) spalling of the protective cement layer in the bridge intrados that was introduced following upgrades performed a few years earlier accompanied by the introduction of a steel mesh in the intrados and (b) loss of parapet sections. A considerable number (16%) of the checked 925 buildings of the town of Konitsa, located at close proximity to the stone masonry bridge, developed structural damage typical to Greek construction [24]. The recorded ground motion (see **Figure 29** of strong motion acceleration [15]) exhibits the characteristics of an impulse-type or near-field earthquake especially its horizontal component that contains the characteristic pulse. This acceleration record, shown in **Figure 29**, is used as bridge base excitation in the non-linear analysis. Three-dimensional excitation was considered for all the seismic analyses performed. For the Konitsa 1996 earthquake analysis, the in-plane and out-of-plane horizontal components were identical and reflected the recorded horizontal acceleration trace of **Figure 29**. The vertical excitation component was the one also shown in **Figure 29**. No SSI considerations were introduced at the bottom of the two abutments, which were assumed to be fixed on rock. Further, for these analyses no differentiation in ground motion between abutment supports was considered despite the fact that one abutment is supported on competent rock and the other in what appears to be weathered rock.

The seismic study was conducted in two steps. Specifically, during the first step, the static conditions of the structure were reached by introducing a fictitiously high global damping. Upon stabilization throughout the structure (see yellow arrow in **Figure 38a**), the earthquake analysis was initiated with the correct damping estimated based on the experimental measurements made during the two campaigns (i.e. global damping of 1.6%, **Figure 38b**). **Figure 39** depicts the state-of-stress profile throughout the Konitsa Bridge due to gravity load

(**Figure 39a** depicts principal deviatoric stress, **39b** vertical stress around the right-hand side (RHS) abutment and **38a** vertical stress evolution during the gravity load analysis reaching stabilization for the start of earthquake analysis).

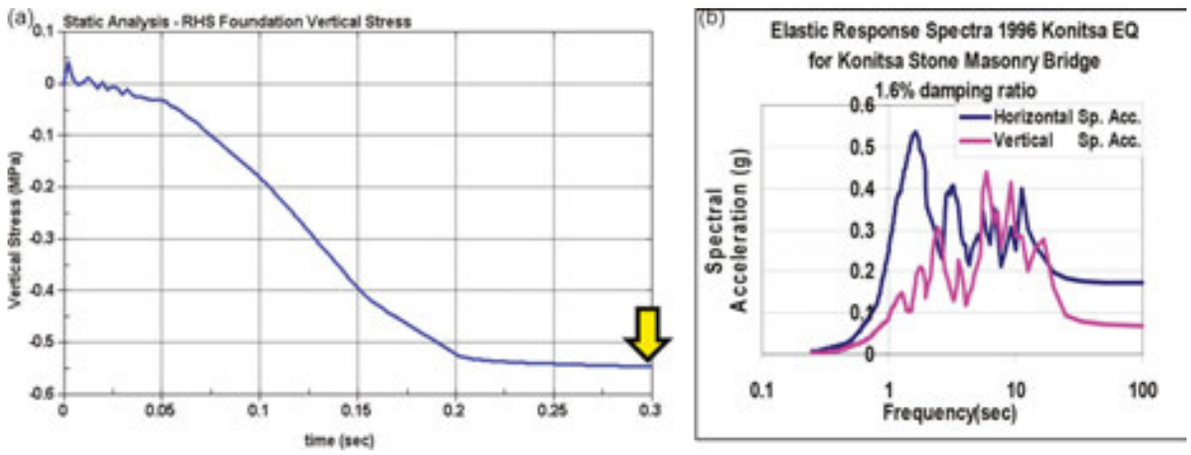

Figure 38. (a) Static state of stresses of Konitsa Bridge at the start of seismic analysis. The arrow indicates the start of the dynamic (earthquake analysis) following the gravity load analysis stabilization. (b) Two percent response spectra of the 1996-Konitsa earthquake recorded on rock.

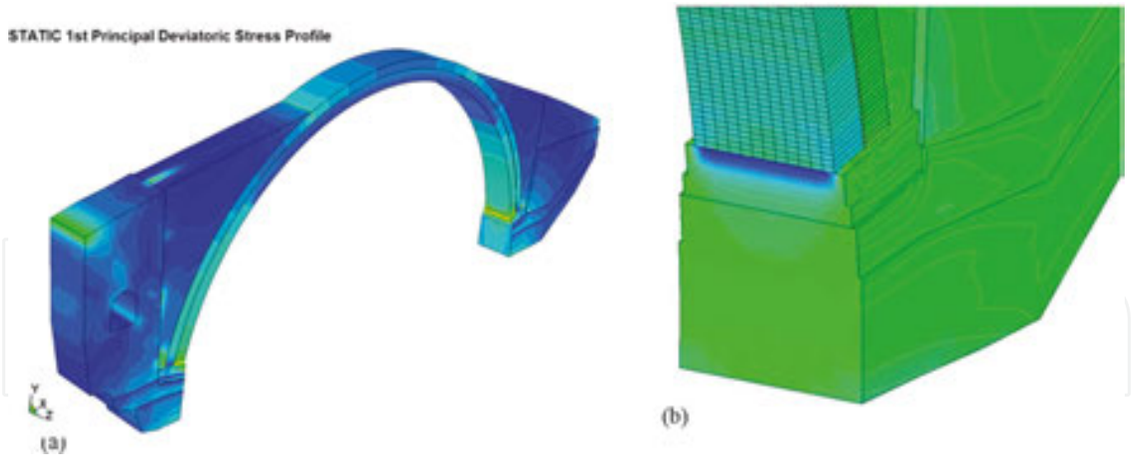

Figure 39. (a) Principal stress profile of Konitsa Bridge under dead load and (b) compressive stress concentration at the foot of the main arch.

Shown in **Figure 40a** is the location of the numerical model of Konitsa Bridge where the seismic response is predicted (crown, Loc-3, Loc-2, Loc-1) having as input motion the described seismic excitation throughout all the base points (Base EQ input). **Figure 40b** depicts the horizontal (in-plane and out-of-plane) and vertical crown displacement seismic response of the Konitsa Bridge predicted using the non-linear numerical analysis. As can be seen in **Figure 40b**, the

http://dx.doi.org/10.5772/64752

maximum predicted out-of-plane horizontal crown displacement is somewhat larger than the maximum value predicted by the linear time-history analysis in Section 7.1 (**Figure 30a**). The maximum predicted in-plane vertical crown displacement (**Figure 40b**) predicted by this non-linear earthquake analysis is significantly larger (approximately four times) than the maximum value predicted by the linear time-history analysis in Section 7.1 (**Figure 30a**). This must be attributed to the fact that the linear analysis performed in Section 7.1 is three-dimensional but employing a numerical model of the bridge that represents its mid-surface, whereas the 3-D non-linear simulation utilizes a model where the bridge is simulated with its actual thickness (compare **Figure 15** with **Figures 35** and **36**). Thus, the vertical displacement at the crown (see **Figure 40a**) predicted by the 3-D non-linear analysis represents the vertical displacement at the façade of the crown cross section of the bridge, which includes a contribution from the out-of-plane response, and not the vertical displacement of the crown at mid-surface, as is the case for the simplified analysis of Section 7.1 (**Figure 30a**). The in-plane horizontal displacement predicted by both the linear and the non-linear earthquake analyses has relatively very small amplitude. As discussed before, this clearly demonstrates the much larger stiffness of the bridge structure along the horizontal in-plane direction than along the out-of-plane direction. In **Figure 41a** and **b**, the absolute velocity response at four locations of the Konitsa Bridge as well as at its base is depicted in the horizontal in-plane or out-of-plane direction, respectively. As can be seen again in these figures, the stiffness of the bridge combined with the applied seismic motion results in very small amplification of this velocity response in the in-plane direction than in the out-of-plane direction between the base and the four Konitsa Bridge locations (Crown, Loc-3, Loc-2, Loc1). This crown/base velocity response amplification factor in the out-of-plane direction has a value approximately equal to 2.

In **Figure 43**, the contours of the effective von-Mises stresses are depicted for the Konitsa Bridge subjected to the previously described 1996-Konitsa earthquake record. As can be seen in this figure, tensile distress is indicated at the right and left ends of the primary and secondary arches where they join the foundation blocks. This is also shown in some detail in **Figure 42a** and **b** in terms of von-Mises and vertical stress response in this location. The time-history plot of the vertical stress at the foundation block (A) at the arch-to-foundation block interface (B) and at the primary arch (C) clearly indicates that the tensile stress at location C reaches, as expected, the largest value, which is in excess of the tensile capacity of the bridge construction material (see also Section 7.1. and **Figure 28e**). By comparing the results of the displacement and stress response of the Konitsa Bridge, as obtained by the present 3-D non-linear analysis, with the corresponding time-history results of the simplified linear analysis of Section 7.1, it can be concluded that the 1996-Konitsa ground motion employed in both cases was of such an intensity and frequency content that very limited non-linearities developed at this 3-D advanced non-linear model of the structure. This conclusion is in line with the observed performance of this bridge during the 1996 main event. As already mentioned before, limited damage was experienced by this bridge in this 1996 earthquake in the form of (a) spalling of the protective cement layer in the bridge intrados that was introduced following upgrades performed few years earlier and (b) loss of parapet sections (**Figure 43**).

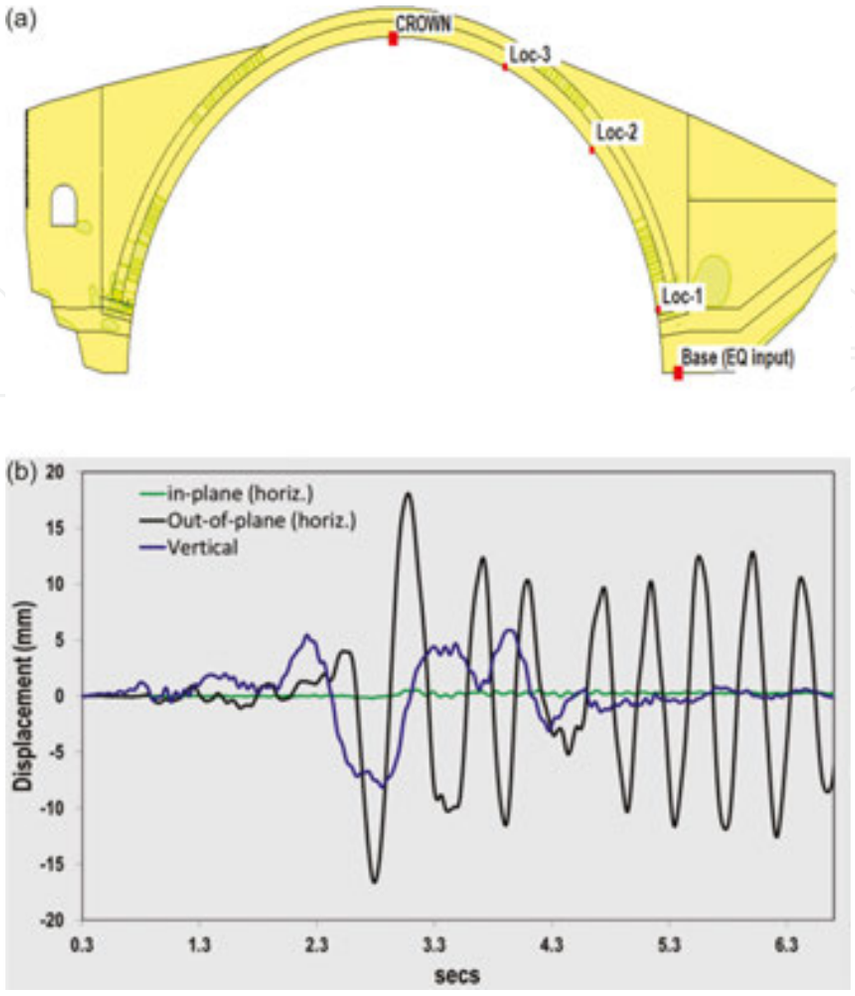

Figure 40. (a) 3-D model of Konitsa Bridge together with the locations of input (excitation) and predicted seismic response and (b) horizontal (in-plane and out-of-plane) and vertical crown displacement seismic response of the Konitsa Bridge predicted using the non-linear numerical analysis.

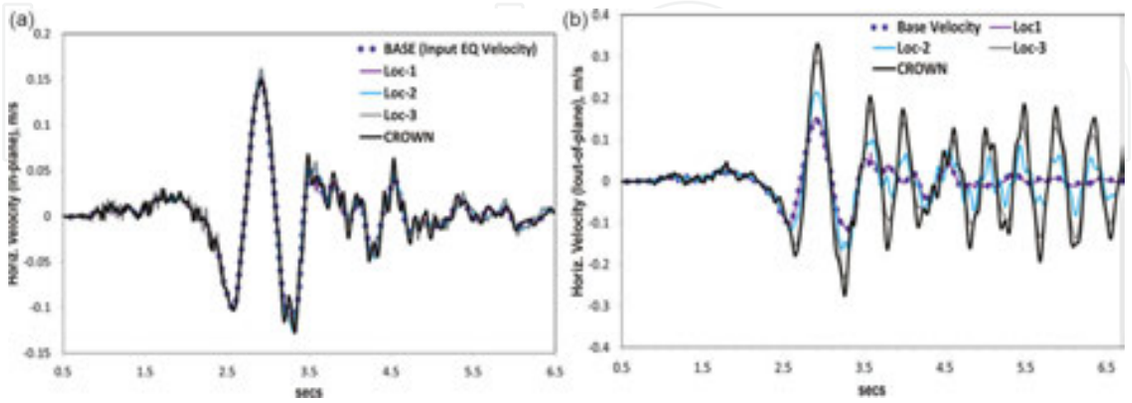

Figure 41. Earthquake response of Konitsa Bridge when subjected to the 3-D 1996-Konitsa earthquake: (a) in-plane horizontal velocities and (b) out-of-plane horizontal velocities.

http://dx.doi.org/10.5772/64752

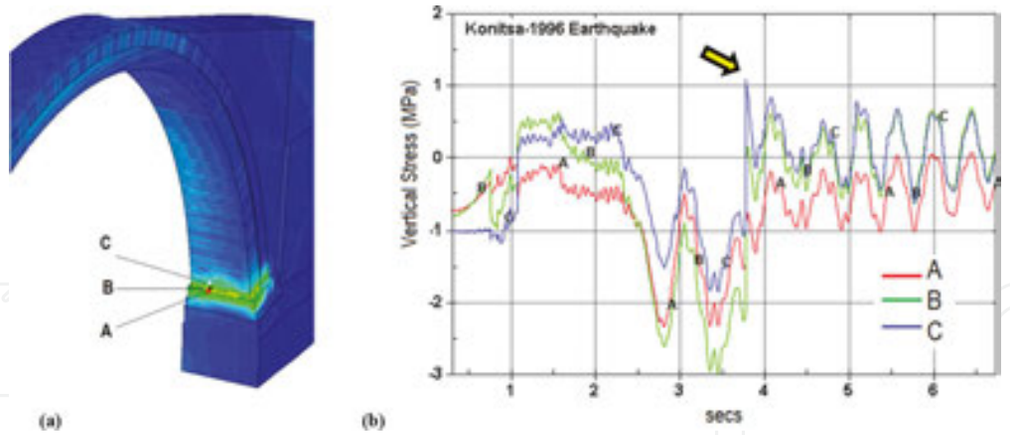

Figure 42. Vertical stress response at the right end of the primary and secondary arches where they join the foundation blocks.

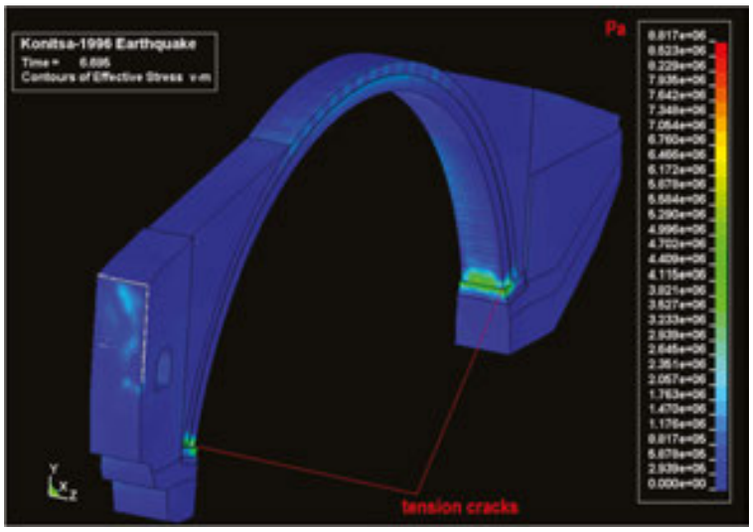

Figure 43. Tensile stress concentration at the foot of the primary and secondary arches of the Konitsa Bridge.

8.4. Seismic vulnerability assessment and code guidance effects

In order to examine the capabilities of the 3-D non-linear numerical simulation performed in the previous section and in an effort to understand the potential influence of the time structure and period content of the exciting earthquake which may be missed when utilizing envelope code spectra (i.e. Euro-Code), the Konitsa Bridge was subjected to two (2) additional earthquakes that represent distinct classes, namely near-field (impulsive-type) and far-field earthquakes. Specifically, the NS component observed at Shiofukizaki site in the 1989 Ito-Oki earthquake of moment earthquake magnitude 5.3, epicentral distance of 3 km and the depth of the seismic source of 5 km. The record was observed at the surface of basalt rock and has a maximum acceleration of 0.189 g. It has been characterized as a near-field earthquake and it exhibits remarkable similarity to the Konitsa 1996 earthquake (**Figure 44**, top).

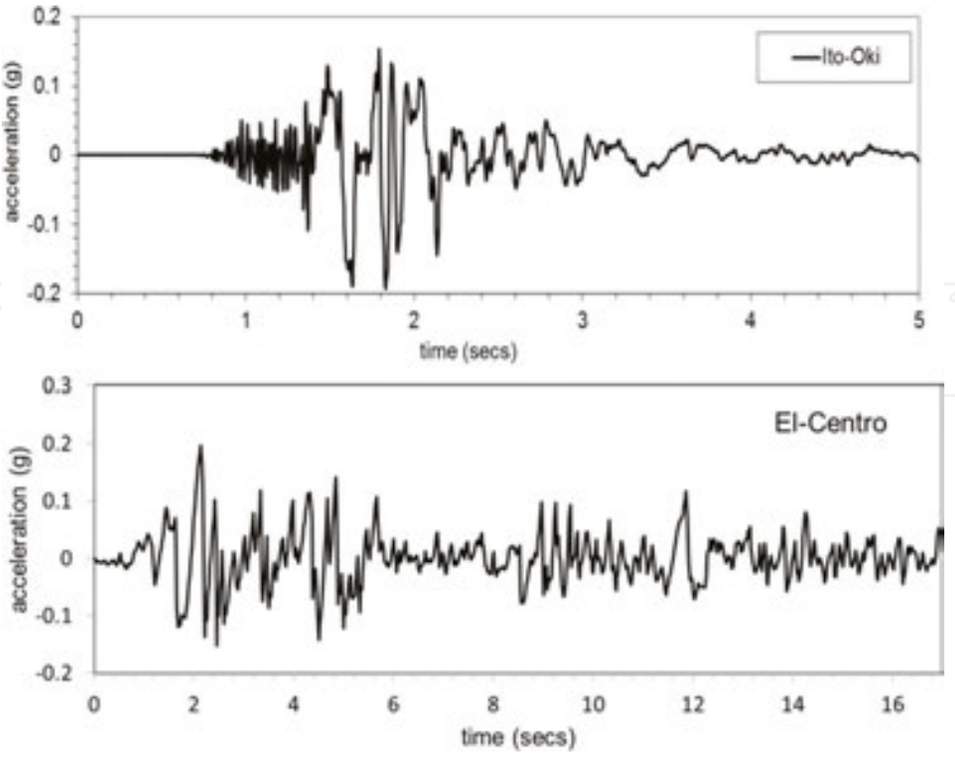

Figure 44. Acceleration time histories of Ito-Oki 1989 and El-Centro1940 PGA-adjusted earthquakes.

The second earthquake is the 1940 El-Centro normalized to 0.19 g (**Figure 44**, bottom) allowing for direct comparison with the similar PGA Konitsa-1996 and Ito-Oki near-field earthquakes. The direct comparison of the response spectra of the three earthquakes (Konitsa-1996, Ito-Oki and normalized 1940 El-Centro) is shown in **Figure 45**. The objective of subjecting the Konitsa Bridge to the same PGA but different spectral content earthquakes is to directly compare the damageability potential based on the non-linear response of the bridge and shed some light on sensitivities to the type of earthquake these type of structures (masonry stone bridges) exhibit. This ultimately will aid in the modification/updating of the seismic codes to capture the unique structural design and response characteristics of large span arch masonry bridges in their provisions. While for the Konitsa-1996 earthquake the actual vertical acceleration was used, for the Ito-Oki and modified 1940 El-Centro the vertical component was assumed as 75% of the employed horizontal component. The results drawn from the three (3) non-linear analyses (Konitsa-1996, Ito-Oki and 1940 El-Centro) and the comparative damageability potential are very revealing. Specifically, very similar response and bridge damage are observed for the two impulsive-type earthquakes, M =5.7 Konitsa-1996 and M = 5.3 Ito-Oki earthquakes, which are similar PGA and time structure. Their damage potential is quite limited and it confirms the observations made post 1996-Konitsa earthquake of the bridge. **Figure 46a** and **b** depict the Konitsa Bridge out-of-plane displacement and stress response, respectively. On this basis and by comparing these maximum response values with the corresponding maximum values obtained utilizing the 1996-Konitsa earthquake record as input motion (**Figures 30a** and **b**, **40b**, **41a** and **b**), it can be concluded that the potential damage vulnerability from the Ito-Oki earthquake resembles that of the Konitsa-1996 earthquake.

http://dx.doi.org/10.5772/64752

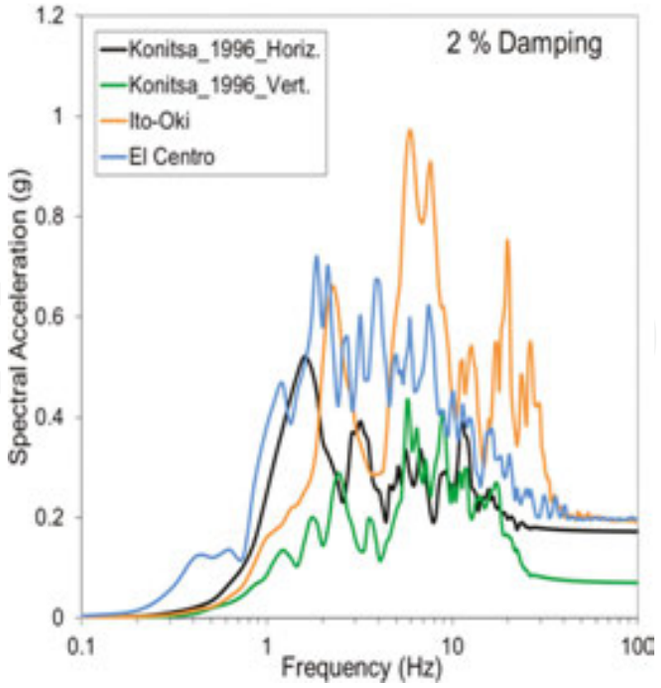

Figure 45. Acceleration response spectra (2% damping) of the similar PGA but different type (near- vs. far-field) earthquakes utilized in the study.

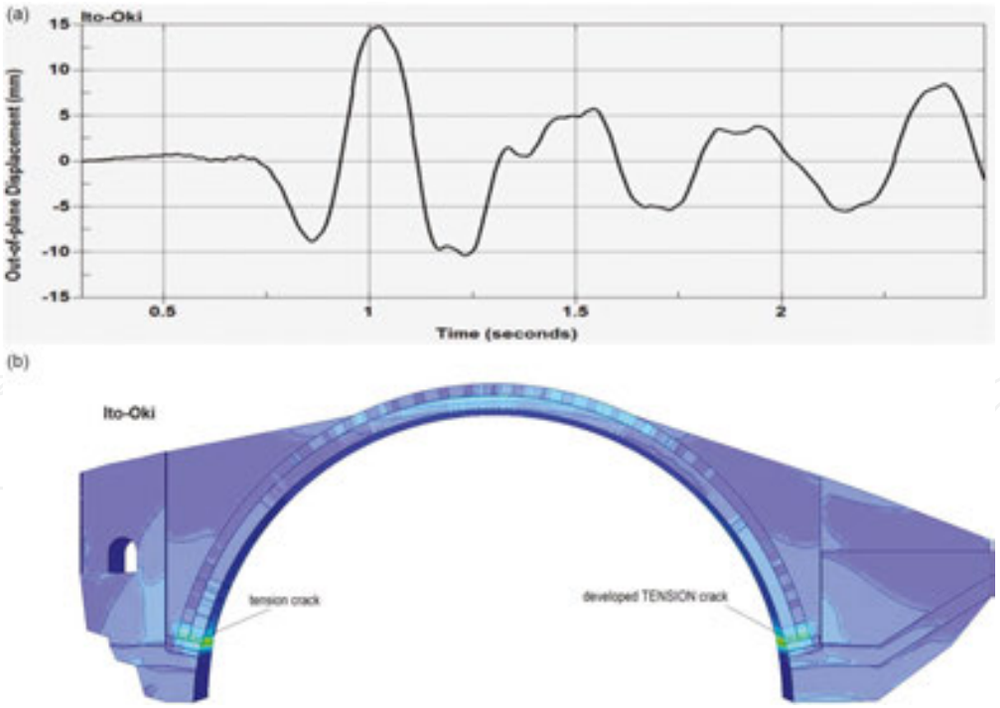

Figure 46. Konitsa Bridge response to the *M* = 5.3 Ito-Oki (0.19g PGA) near-field (impulsive) earthquake. (a) Out-of-plane displacement response and (b) tensile stress response.

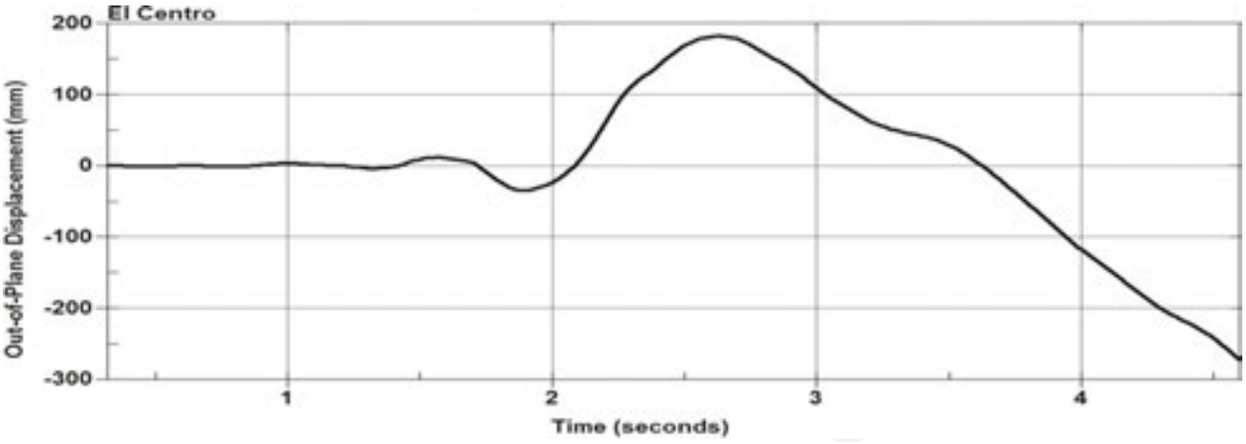

Figure 47. Konitsa Bridge out-of-plane displacement response to PGA-adjusted (0.19 g) 1940 El-Centro earthquake.

A strikingly different bridge response and damage potential are observed when Konitsa Bridge is subjected to an excitation with the 0.19-g normalized 1940 El-Centro earthquake, which represents a different type (far-field) of seismic event lacking that characteristic dominant velocity pulse (**Figure 29**). **Figures 47** and **48** clearly demonstrate the different damage potential of this type of earthquake on such relatively long-span stone-masonry bridges. **Figure 47** depicts the Konitsa Bridge out-of-plane displacement response when subjected to PGA-adjusted (0.19-g) 1940 El-Centro earthquake. **Figure 48** depicts the variation of tensile stresses together with relevant non-linear deformations of large amplitude at critical locations of the main arch during certain time windows of the response when these deformations are maxi-

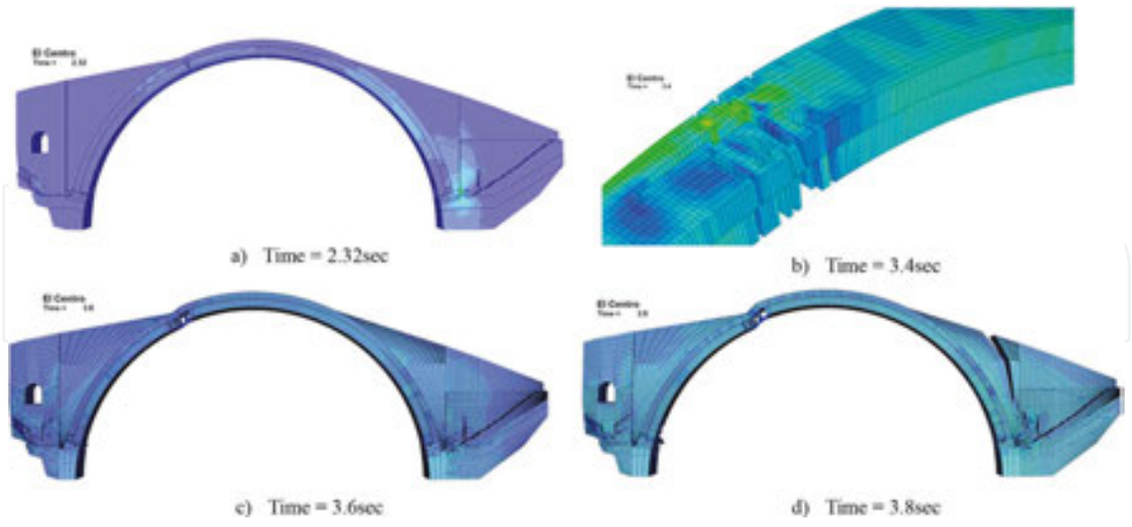

Figure 48. Evolution of damage resulting from the El-Centro (0.19-g) far-field-type earthquake. (a) Time = 2.32 s, (b) 3.4 s, (c) 3.6 s and (d) 3.8 s.

mized, thus indicating the collapse potential of that portion of the main arch. This prediction of the main arch performance is in agreement with a similar conclusion reached by the simplified analyses of Section 7.1 when Konitsa Bridge (**Figures 27b**, **28b** and **d**) and Plaka Bridge (**Figures 33** and **34**) were subjected to the design spectra as defined employing provisions of Euro-Code 8. This large variation in the damageability potential, therefore, should be accounted for in establishing seismic code guidelines for relatively fragile old cultural heritage structures (as the old stone-masonry bridges studied in this chapter) as they apply to these non-typical structures. It should be noted that similar conclusions regarding the damageability of near-field-type earthquakes, as compared to their far-field counterparts based on which seismic codes for nuclear structures were deduced, were reached following an International Atomic Energy Agency (IAEA)-launched coordinated research project (CRP) experimental study [23] augmented with numerical analysis and response/damage predictions conducted by an international participation.

9. Maintenance issues for stone-masonry bridges

In this section, a brief discussion will be presented dealing with maintenance issues of the stone-masonry bridges that were examined in this chapter. This study focused on the dynamic and seismic response of this type of bridges. However, it was shown by past experience that structural damage can also result from other types of actions such as flooding or traffic when such bridges are used not only for light pedestrian use. Because almost all the stone-masonry bridges in Greece have been built mostly for relatively light live load levels resulting from the crossing of pedestrians or animal flocks, their structural vulnerability due to traffic conditions is not an issue. Instead, flooding of the narrow gorge currents that these bridges cross (**Figure 49a**) is one of the main structural damage causes, as demonstrated from the Plaka Bridge (see **Figure 50a** and **b**). Apart from the hydrodynamic loads that a stone-masonry bridge is subjected to from a flooded current, one of the main sources of distress that may lead to partial or total collapse is the deformability of the foundation. The deformability of the foundation and the potential for subsequent collapse does include not only wash-out effects from a sudden flooded current but also the cumulative deformability of the foundation in a wider time

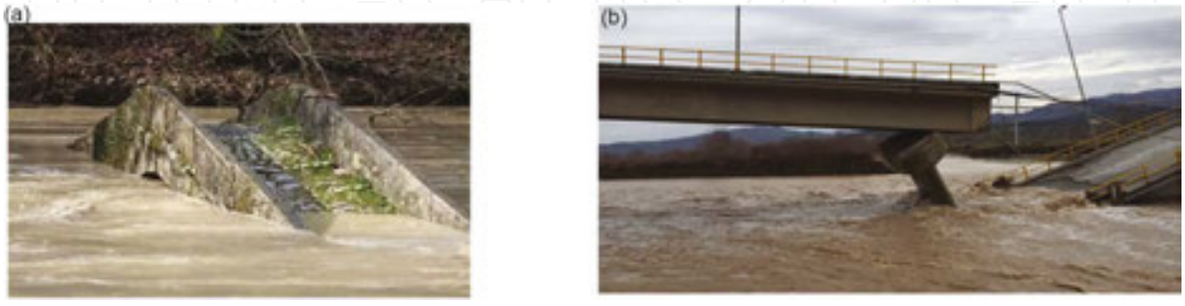

Figure 49. (a) Almost total flooding of a stone masonry bridge and (b) tilting of a mid-pier and partial collapse of the Diava-Kalampaka reinforced concrete bridge in Thessaly, Greece (16th January, 2016).

window as was demonstrated by a recent flooding of Pineios river that caused the tilting of a mid-pier and the partial collapse of the Diava-Kalampaka-reinforced concrete bridge in Thessaly, Greece (16 January 2016, **Figure 49b**).

Figure 50. (a) View of the Plaka Bridge after the collapse from the West bank. Note the total destruction of the mid-pier (see also **Figure 7d**). (b) Close-up of the total destruction of the mid-pier of Plaka Bridge (see also **Figure 7d**).

Thus, foundation maintenance seems to be of the utmost importance. The flooding of Arachthos river, which caused the collapse of Plaka Bridge on 31 January 2015, was of considerable proportions. It is of interest to observe the conditions of the mid-pier of Plaka Bridge after the collapse (**Figure 50a** and **b**). As can be seen, the foundation of this pier is almost non-existent being covered by the remains of the East part of central arch and of part of the adjacent arch and mid-pier. Thus, it is evident that this mid-pier was highly distressed leading to this mode of collapse.

Another maintenance issue of considerable importance is the integrity of the stone masonry in parts of the bridge apart from the foundation. It was already discussed in Section 6, when comparing numerically predicted with measured eigen-frequency values, that evidence of washed-out mortar joints was present mainly in Kontodimou, Tsipianis and Kokorou Bridges. At the time of *in situ* measurements (October to December 2015), maintenance works took place in Konitsa Bridge focusing on the removal of vegetation and re-pointing of the mortar joints. The effectiveness of these operations must be validated through laboratory testing regarding the compatibility and durability of the materials employed. The presence of metal ties and their structural function was underlined in Section 3. However, inspection of these metal ties in the stone-masonry bridges of the present study as well as other stone-masonry bridges not reported here casts doubts on their effectiveness due to lack of maintenance for a long time.

In some cases, these stone-masonry bridges suffered structural damage from human activity. Plaka Bridge is one such example as can be seen in **Figure 51a**. The red arrow in this figure points to the structural damage suffered by the central arch due to an explosion during World War II. The damaged part was retrofitted in a way that is not known in detail to the authors. This retrofitting is visible in detail in **Figure 51b** where one can distinguish the difference in the texture of the old stone masonry from the retrofitted part of the secondary arch in this location indicated by the red circle.

http://dx.doi.org/10.5772/64752

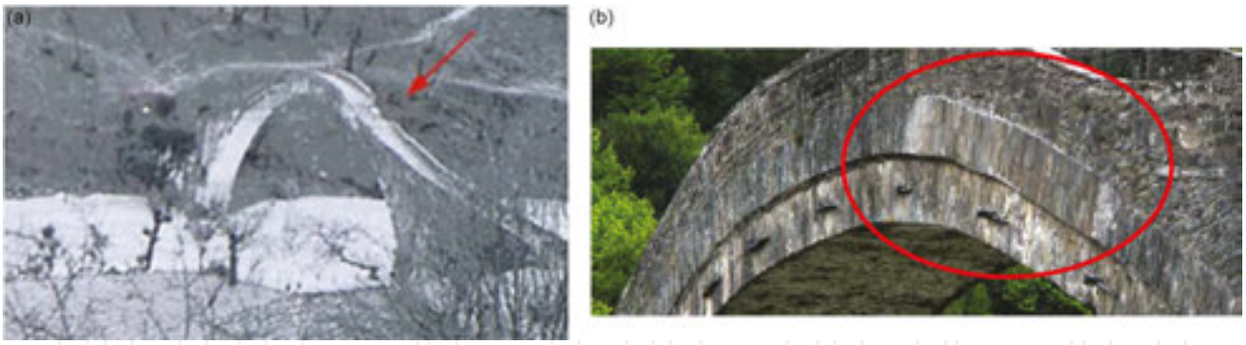

Figure 51. (a) Structural damage at the East part of the central arch of Plaka Bridge due to an explosion. (b) Detail of the retrofitted part of the secondary arch of the Plaka Bridge sometime before its collapse from flooding.

This is also visible in **Figure 52a** where the scaffolding used for additional maintenance works is also visible. However, these works did not prove sufficient to prevent the collapse of this bridge from the severe flooding. It is of great research interest to be able to apply the methodology of *in situ* investigation presented in Section 4 of this chapter together with a long-term monitoring and maintenance programme as means of safeguarding the structural integrity of these precious cultural heritage structures.

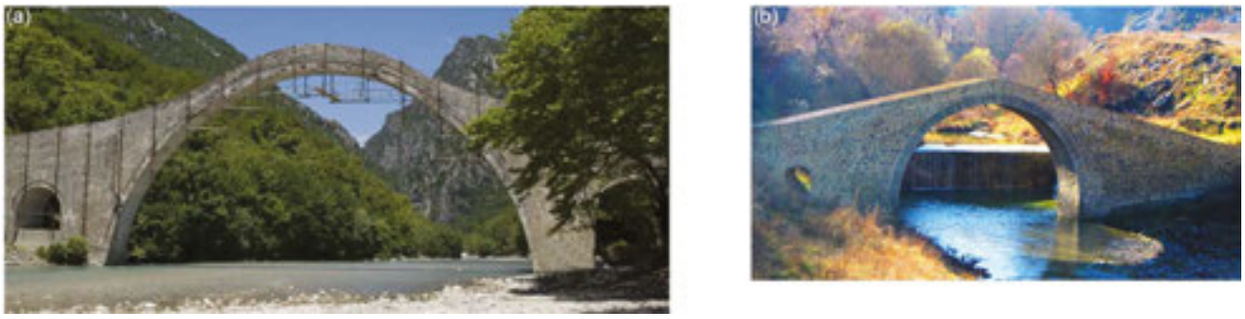

Figure 52. (a) Maintenance works at Plaka Bridge sometime before its collapse from flooding and (b) stone-masonry bridge at Dasilio-Grevena, Greece after being retrofitted.

In the brief space of this section, the principles that govern a major retrofitting of such bridges must also be underlined. This is very important not only for the collapsed Plaka Bridge and the plans for its reconstruction but for numerous other bridge structures that have suffered serious structural damage or partial collapse. **Figure 52b** depicts a stone-masonry bridge in North-Western Macedonia, Greece, which underwent major reconstruction. It is worth mentioning that the regions of North-Western Macedonia and Ipiros in Greece are the home of stone masons who have been active worldwide. Due to their initiative specific stone-masonry workshops have been established recently in this region in an effort to keep this type of traditional construction as well as its maintenance alive.

10. Conclusions

This structural performance of old stone-masonry bridges is studied following a methodology that utilizes a large number of high fidelity *in situ* measurements in order to identify their dynamic characteristics (eigen-frequencies, eigen-modes and damping ratio) and corresponding numerical predictions from relatively simple or more complex numerical simulations. The validity of these numerical simulations was ascertained by comparing the measured *in situ* dynamic response with the one predicted numerically. This methodology was extended by applying such 'realistic' numerical simulations to predict the performance of specific old stone-masonry bridge structures (e.g. Konitsa Bridge) when subjected to dead load combined with seismic actions. A series of numerical dynamic analyses, both simplified (linear) and complex (non-linear), were made. In these analyses, actual earthquake excitation recorded in the proximity of Konitsa Bridge and relevant seismic code design seismic spectra were employed as well as earthquake records representing near-field (impulsive-type) or far-field seismic events. Seismic actions specified in these ways were used to investigate the damage potential of such stone-masonry bridges. It is believed that it is of great research interest to be able to apply this methodology together with measurements from a long-term monitoring and maintenance programme as a means of safeguarding the structural integrity of these precious cultural heritage structures. Finally, recommendations for intervention works should include clauses providing for preparatory actions of measurements and analyses similar to the methodology presented here. The same methodology can be applied to address flooding, which is also one of the main causes of structural damage for stone-masonry bridges that require special attention and is the subject of a separate study. Apart from the hydrodynamic loads that a stone-masonry bridge is subjected to from a flooded current, one of the main sources of distress that may lead to partial or total collapse is the deformability of the foundation. Finally, the integrity of the stone masonry in various parts of such old stone-masonry bridges is an additional maintenance issue of considerable importance. The following represent additional conclusive remarks:

1. The numerically predicted bridge deformation and stress state seismic response are in good agreement resulting from either the simple or complex numerical simulations as well as with observed structural performance following actual earthquake occurrence in the proximity of Konitsa Bridge. This offers confidence in the described methodology using (a) detailed modelling which incorporates both field measurements of the dynamic characteristics and (b) laboratory testing on the complex mortar-stone mechanical behaviour in its aged/weathered condition.

2. The high fidelity of the complex non-linear numerical analyses that were used to predict the vulnerability of these structures to earthquakes and account for new fault information that surfaces in the proximity of these structures should also be underlined. The influence of certain issues that were not included in the current numerical treatment, such as soil-structure interaction, deformability of the foundation, and so on, should also be addressed in the future. This vulnerability analysis demonstrated:

- The damage potential of far-field earthquakes on these types of unique structures (long-span masonry stone) is far greater than the damageability of impulsive-type earthquakes. This is confirmed through detailed analysis of the Konitsa Bridge using actual impulsive and far-field seismic records.
- The observations on the damageability variation between impulsive- and far-field earthquakes confirm previously conducted experimental and numerical studies on nuclear structures.
- The above findings should be considered in establishing seismic code guidelines to specifically apply to these structures considering that they are typically constructed to span river beds that are in turn closely related to faulting [25].

Acknowledgements

- The assistance of D. Gravas, K. Giouras and C.G. Manos junior in conducting the field experiments and gathering geometric information relevant to the stone-masonry bridges presented here as well as the help of the local people is gratefully acknowledged.
- For conducting the laboratory tests, we would like to thank T. Koukouftopoulos and V. Kourtidis from the laboratory of Strength of Materials and Structures of Aristotle University.
- Finally, we would also like to thank J. Evison Manou for editing this manuscript.

Author details

George C. Manos[1*], Nick Simos[2] and Evaggelos Kozikopoulos[1]

*Address all correspondence to: gcmanos@civil.auth.gr

1 Laboratory of Experimental Strength of Materials and Structures, Department of Civil Engineering, Aristotle University of Thessaloniki, Thessaloniki, Greece

2 Brookhaven National Laboratory, Upton, NY, USA

References

[1] O'Connor C., (1993), Roman bridges, Cambridge University Press, ISBN 0-521-39326-4.

[2] Grassos G. Editor, (2007), The stone masonry arch bridges of Greece, Center of Environmental Education, Makrinitsas, ISBN: 978-960-98043-9-4 (in Greek). http://kpemakrin.mag.sch.gr. Published by Eptalofos, www.eptalofos.gr.

[3] Psimarni K., Georgopoulos A., Balodimos D.D. (2000), "Development of a geographic information system for the traditional bridges of central Zagori", Report to the Municipality of Zagori, in Greek.

[4] Aoki T., et al, (2007), "Theoretical and experimental dynamic analysis of Rakanji Stone Arch Bridge, Honyabakei, Oita, Japan," 7th International Conference on Motion and Vibration Control, MOvIC 04.

[5] Sevim Barıs, et al., (2011), "Finite element model calibration effects on the earthquake response of masonry arch bridges," Finite Elements in Analysis and Design, 47 (2011), 621–634.

[6] G. C. Manos G.C., Pitilakis K.D., A. G. Sextos A.G., V. Kourtides V., Soulis V., and Thauampteh J., (2015), "Field Experiments for Monitoring the Dynamic Soil–Structure–Foundation Response of a Bridge-Pier Model Structure at a Test Site", J. Struct. Eng. 141(1), D4014012; http://dx.doi.org/10.1061/(ASCE)ST.1943-541X.0001154.

[7] Manos G.C. and Kozikopoulos E., (2015), "In-situ measured dynamic response of the Bell Tower of Agios Gerasimos in Lixouri-Kefalonia, Greece and its utilization of the numerical predictions of its earthquake response", COMPDYN 2015, Greece, 25–27 May 2015.

[8] Ozden Caglayan B., Kadir Ozakgul and Ovunc Tezer, (2012), "Assessment of a concrete arch bridge using static and dynamic load tests", Structural Engineering and Mechanics, Vol. 41, No. 1 (2012), 83–94.

[9] Simos N. and Manos G.C., "Earthquake Vulnerability of Stone Arch Bridges using Non-linear Finite Elements and Measurements of Dynamic Characteristics," *Engineering Structures*, 2016 (submitted, in-review).

[10] Simos N. and Manos G.C, (2013), "Numerical analysis of seismic response of natural stone arch bridges-field observations and a case study," COMPDYN 2013, http://www.eccomasproceedings.org/cs2013/.

[11] Manos G.C. and Kozikopoulos E., (2015), "The dynamic and earthquake response of basilica churches in Kefalonia, Greece including soil-foundation deformability and wall detachment", COMPDYN 2015, Greece, 25–27 May 2015.

[12] Eurocode 8 – Design of structures for earthquake resistance – Part 2: Bridges, DRAFT, No. 3. European Committee for Standardization; Management Centre: rue de Stassart, 36 B-1050 Brussels, 2004.

[13] Provisions of Greek Seismic Code 2000, OASP, Athens, December 1999. Revisions of seismic zonation introduced in 2003.

[14] Paz. M., (1994), *International Handbook of Earthquake Engineering:* "Codes, Programs and Examples", edited by Mario Paz, Chapter 17, Greece by G.C. Manos, Chapman and Hall, ISBN 0-412-98211-0, 1994.

[15] Institute of Engineering Seismology and Earthquake Engineering (ITSAK), Data Base of Greek Earthquake Strong Motions, http://www.itsak.gr/en/head.

[16] Manos G.C., Kotoulas L., Soulis V., Felekidou O., (2015), "Numerical simulation of the limit non-linear behaviour of unreinforced masonry under in-plane state of stress from gravitational and seismic actions", COMPDYN 2015, Greece, 25–27 May 2015.

[17] Kiyono J., et al., (2012), "Seismic Assessment of Stone Arched Bridges," 15 WCEE, Lisbon, Portugal, 2012.

[18] Drosopoulos G.A., Stavroulakis G.E., Massalas C.V., (2006), "Limit analysis of a single span masonry bridge with unilateral frictional contact interfaces," Engineering Structures 28 (2006) 1864–1873.

[19] Korompilias D., (2015), "Study of the inelastic behaviour of the Konitsa Bridge using an inelastic model for masonry and applying strengthening methods," PhD Thesis, University of Patras, Greece, 2015 (in Greek).

[20] LS-DYNA-Version 9.71, Livermore Software Technology Corp. – LSTC, True-Grid-Version 2.3.4, XYZ Scientific Applications, Inc.

[21] Papanastasiou D., (2001), "The Konitsa, Epirus NW Greece, July 26 (Ms = 5.4) and August 5, 1996, (Ms = 5.7) earthquakes sequence", Bulletin of the Geological Society of Greece, XXXIV, 1555–1562.

[22] Spyrakos C.C., Maniatakis C.A. and Taflambas J., (2008), "Evaluation of near-source seismic records based on damage potential parameters: Case study: Greece", Soil Dynamics and Earthquake Engineering 28 (2008) 738–753.

[23] Non-linear Response to a Type of Seismic Input Motion, IAEA-TECDOC-1655-ISSN 1011-4289, June 2011.

[24] Manos G.C., (2011), "Consequences on the urban environment in Greece related to the recent intense earthquake activity", International Journal of Civil Engineering and Architecture, December, Vol. 5, No. 12 (Serial No. 49), pp. 1065–1090.

[25] Galanakis D., Paschos P., et al., (2007), "Neotectonic Activity of Konitsa Area and the 1996 Earthquakes", Hellenic Journal of Geosciences, Vol. 42, 57–64.

IntechOpen